THE GEOLOGICAL SOCIETY OF AMERICA®

Post-collisional Cenozoic extension in the northern Aegean: The high-K to shoshonitic intrusive rocks of the Maronia Magmatic Corridor, northeastern Greece

Rebecca J. Perkins[1], Frances J. Cooper[1], Daniel J. Condon[2], Brian Tattitch[1], and Jonathan Naden[2]
[1]SCHOOL OF EARTH SCIENCES, UNIVERSITY OF BRISTOL, WILLS MEMORIAL BUILDING, QUEENS ROAD, BRISTOL BS8 1RJ, UK
[2]BRITISH GEOLOGICAL SURVEY, NICKER HILL, KEYWORTH, NOTTINGHAM NG12 5GG, UK

ABSTRACT

The Maronia Magmatic Corridor is a NE-trending belt of Oligocene plutons that intrudes the Kechros Dome of the northern Rhodope Core Complex in northeastern Greece. The post-collisional magmatism transitions from early high-K calc-alkaline magmatism in the NE to a younger, shoshonitic phase in the SW. We use a full suite of whole-rock geochemical analyses, including rare earth elements, to show a shared metasomatized mantle source of the magmatism. Evidence of plagioclase saturation from the onset of crystallization and amphibole-pyroxene-controlled fractionation in the high-K calc-alkaline magmatism suggest a drier (<4.75 wt% H_2O) parental magma than is typical of subduction-related magmatism. Continued H_2O depletion of the metasomatized source mantle resulted in the transition to a shoshonitic trend where deep crustal fractionation of an H_2O-poor (< ~2 wt% H_2O) magma in the absence of major olivine resulted in incompatible enrichment over a small range of SiO_2. High-precision U-Pb zircon geochronology is presented here for the first time to provide chronological markers for the transition in the magmatic evolution of the Kechros dome. A 2.2 Myr break in magmatism separates the intrusion of the shoshonitic Maronia pluton at 29.8 Ma from the emplacement of the rest of the high-K calc-alkaline Maronia Magmatic Corridor between 32.9–32.0 Ma. The Maronia pluton is the hottest, driest, and youngest episode of post-collisional magmatism in the Kechros dome; we suggest that the emplacement of Maronia marks the cessation of magmatism in the northern Rhodope Core Complex as asthenospheric mantle upwelling migrated southward.

LITHOSPHERE; v. 10; no. 5; p. 582–601; GSA Data Repository Item 2018177 | Published online 15 June 2018 https://doi.org/10.1130/L730.1

INTRODUCTION

Mountain-building events can generate thousands of kilometers of high elevation over periods of tens to hundreds of millions of years; the development of such high relief during orogenesis is supported by the development of a thick continental root (e.g., Dewey et al., 1993). In some orogens this crustal thickness is preserved long after collision, while in others post-collisional collapse of the orogen thins the crust and results in widespread extensional structures that dissect the region (e.g., Le Pichon and Angelier, 1979; Dewey, 1988; Wang et al., 2014). In extended orogens, strain localization can drive the formation of trans-crustal normal detachment faults that transfer material from the ductile, lower crust to the surface and can aid the exhumation of metamorphic core complexes from >45 km depth (e.g., the North American Cordillera: Coney, 1987; Wernicke et al., 1987; Camp et al., 2015; and the Aegean: Lister et al., 1984; Jolivet and Brun, 2010; Burg, 2011; Kydonakis et al., 2015). Another feature of highly extended orogenic terranes is the ubiquitous presence of post-collisional magmatism. The conductive transfer of heat from upwelling hot, asthenospheric mantle beneath highly extended crust can generate small volume, partial melts that exploit crustal pathways developed during extensional deformation, leading to intrusive and extrusive post-collisional magmatism (e.g., McKenzie and Bickle 1988; von Blanckenburg and Davies 1995). Feedbacks between metamorphic core complex exhumation and magmatism are numerous and include magmatic volatiles facilitating crustal deformation and crustal thinning and resultant decompression and mantle upwelling, driving lithospheric melting (Teyssier and Whitney, 2002; Whitney et al., 2013; Platt et al., 2015). As a result, both metamorphic core complexes and post-collisional magmatic suites can be used to offer insights into the tectonic processes controlling crustal extension; here we focus on the petrogenesis of post-collisional magmatism.

In collisional orogenic belts, subduction-related calc-alkaline magmatism shows a trend of increasing K with maturity of the magmatic system (e.g., Lipman et al., 1972). The transition from high-K calc-alkaline to shoshonitic magmatism is common in post-collisional tectonic settings where the inherited metasomatized mantle wedge is depleted at the onset of magmatism (e.g., Aldanmaz et al., 2000; Seghedi et al., 2004). This high-K calc-alkaline to shoshonitic evolution in magma geochemistry is observed throughout the Aegean—for example, in the Eocene to middle-Miocene Biga orogenic rocks in NW Turkey and the Oligocene and Miocene magmatic rocks of NE and central Greece (e.g., Maronia, Samothraki, Lesbos and Limnos) (Del Moro et al., 1988; Pe-Piper et al., 2009; Ersoy et al., 2017).

The generation of potassic melts from the mantle is widely ascribed to be the result of anomalously hot mantle melting (Gill 1981). Source mantle geochemistry is also widely considered to be key in the generation

of potassic to ultra-potassic fractionation trends in subduction-related settings (e.g., Foley et al., 1987). However, the origin of a K-rich source mantle is debated; current hypotheses include, but are not limited to, (i) intense mantle metasomatism by K-rich fluids from the dehydrated, downgoing slab (e.g., Poli and Schmidt, 2002; Condamine and Médard, 2014); and (ii) contamination and physical mixing of mantle melts and lower crustal or subducted sedimentary melts (e.g., Beccaluva et al., 2013; Wang et al., 2017). In addition to source mantle geochemistry, conditions of magma generation and fractionation are also considered to be important in the production of potassic to ultra-potassic magmas (e.g., Peccerillo et al., 2013). Experimental and geochemical studies have shown that magmas generated at high pressures and temperatures, in the absence of abundant H_2O, can produce shoshonitic liquid lines of descent (LLDs) by stabilizing pyroxene and anorthite-rich plagioclase over olivine in the fractionating assemblage, and that the same magmas generated under shallower or more fluid-rich conditions would fractionate a high-K calc-alkaline trend (Meen, 1987; Freise et al., 2009; Lanzo et al., 2016; Beermann et al., 2017). While all of these models require an elevated mantle geotherm to generate high-temperature mantle melts, the mechanism by which a shoshonitic fractionation trend is achieved has important implications for the conditions of magma petrogenesis.

The Hellenic Orogen (or Hellenides) is a 500-km-long mountain belt that stretches across the Aegean and is bound by the Balkanides in the north and the Hellenic trench, the point of present subduction of the African plate beneath Eurasia, in the south (Smith and Moores, 1974; Mountrakis, 2006). Resulting from closure of the Tethys Ocean and subsequent collision of the African and Eurasian plates, the Hellenic orogen is a well-studied example of post-collisional extension. Predominantly attributed to retreat of the Hellenic trench and roll back of the African Slab, Hellenic extension is also thought to incorporate elements of lithospheric delamination and slab break-off beneath Anatolia to the east of the Aegean (Jolivet and Brun, 2010; Ring et al., 2010; Burg, 2011; Brun et al., 2016, and references therein). Terrane accretion and subduction of intermediate oceanic crust (the Vardar-Izmir and Pindos basins) during the Hellenic Orogen began in the late Cretaceous and continued into the Cenozoic (e.g., van Hinsbergen et al., 2005; Schmid et al., 2008). Post-collisional orogenic collapse of the Hellenides began in the late Mesozoic to Cenozoic, contemporaneous with continued north-dipping subduction further toward the south, and has been irregular both spatially and temporally ever since (e.g., Jolivet and Brun, 2010; Ring et al., 2010).

A two-stage model for Aegean extension was developed to accommodate localized Paleogene extension in NE Greece and distributed Neogene extension across the rest of the region (Jolivet and Brun, 2010; Brun et al., 2016, and references therein). This paper focuses on localized tectonic extension in NE Greece where an early phase of trans-crustal extension accommodated exhumation of the northern Rhodope core complex (RCC) from mid- to lower-crustal levels (e.g., Burg, 2011; Kydonakis et al., 2014). Later Neogene extension in the northern RCC was restricted to the upper crust and the formation of normal fault-bound sedimentary basins (e.g., Burchfiel et al., 2003; Kilias et al., 2013). The Maronia Magmatic Corridor (MMC), an 150-km-long NE-trending belt of post-collisional Oligocene calc-alkaline to shoshonitic plutons, intrudes the Kechros dome at the eastern margin of the northern RCC (Del Moro et al., 1988). In this paper, we present detailed field and petrographic observations and new whole-rock geochemistry, including a full suite of rare earth elements (REEs), of the MMC to better constrain the petrogenesis of the potassic post-collisional magmatism. We use field observations coupled with chemical abrasion–isotope dilution–thermal ionization mass spectrometry (CA-ID-TIMS) U-Pb zircon geochronology and whole-rock geochemistry of the plutons to constrain crystallization to within tens of thousands of years, to investigate the temporal evolution of the MMC, and to discuss how geochemical changes in magma petrogenesis relate to the timing of Cenozoic post-collisional orogenic collapse in the northern RCC.

GEOLOGICAL SETTING

The Rhodope Massif is located in the northern Aegean, straddling the border between northern Greece and southern Bulgaria (Fig. 1). The rocks of the Rhodope Massif have a long and complex tectonic history associated with terrane accretion during the Hellenic orogeny and subsequent core complex formation and exhumation (e.g., Ricou et al., 1998). A series of stacked nappes, the Rhodope Massif can be split into two tectonic domains, the northern RCC and the southern RCC, separated by the Nestos thrust (Fig. 1A). The northern and southern RCC have a shared history during terrane accretion in the Mesozoic, but the evolution of the tectonic units diverged during Cenozoic exhumation (e.g., Kydonakis et al., 2014).

Convergent Orogenesis and Metamorphism

The Rhodope Massif has a broadly anticlinal structure and can be subdivided into three lithological units: (i) the lower Pangaion (or Thracia or Drama) terrane of ortho- and para-gneisses, exposed in the core of the fault-bound anticlinal domes (Krohe and Mposkos, 2002; Turpaud and Reischmann, 2010; Burg, 2011; Bonev et al., 2013); (ii) the overlying, upper Rhodope unit, a metaophiolite-gneiss-schist assemblage in the hanging wall of the Rhodope anticline (Krohe and Mposkos, 2002; Burg, 2011); and (iii) the highly deformed imbricate unit sandwiched along the Nestos suture zone between the upper and lower terranes (Bauer et al., 2007; Krenn et al., 2010). In the southern RCC the upper terrane is preserved in the hanging wall of the Kerdyllion fault (Fig. 1A). In the northern RCC lower terrane gneiss domes dominate; in the east, the greenschist facies Mesozoic schist units of the Circum Rhodope Belt (CRB) are considered to be equivalents of the upper Rhodope terrane hanging wall (Bonev and Stampfli, 2008; Krenn et al., 2010; Meinhold et al., 2010; Bonev and Stampfli, 2011; Meinhold and Kostopoulos, 2013).

Considerable geochronological effort, in tandem with detailed microstructural and tectonic contextual study, has been put into unravelling the tectono-metamorphic evolution of the Rhodope Massif (synthesized in Fig. 1B; Table 1). Variscan-age rift-related igneous protoliths in the lower, Pangaion, and upper, Rhodope, terranes indicate a shared, European basement affinity of the tectonic units that make up the Rhodope Massif (Turpaud and Reischmann, 2010; Burg, 2011, and references therein). Jurassic–Cretaceous igneous protoliths in the imbricate unit record subduction-related magmatism on the Rhodopean margin as the rift-basin that separated the Rhodope and Pangaion terranes in the early Mesozoic was closed (e.g., Schmid et al., 2008; Turpaud and Reischmann, 2010; Burg, 2011). This period of subduction is also recorded by diamond- and coesite-bearing ultra-high pressure (UHP) metamorphism, as lenses of the imbricate unit were buried along the Nestos suture zone between 180–160 Ma (Mposkos and Kostopoulos, 2001; Bauer et al., 2007; Krenn et al., 2010); this was co-incident with obduction of the Evros ophiolite onto the Rhodope terrane (Bonev et al., 2015). Greenschist facies metamorphism of the CRB was contemporaneous with the accretion of the Pangaion terrane and ophiolite obduction (Bonev et al., 2013, 2015). In the late Cretaceous, following the underthrusting of the Pangaion terrane beneath the Rhodope terrane, subduction of the Vardar-Izmir Ocean initiated to the south of the Rhodope Massif (e.g., van Hinsbergen et al., 2005; Schmid et al., 2008). Aegean extension initiated in the Rhodope Massif in the Cenozoic during a transitional tectonic period from subduction-related

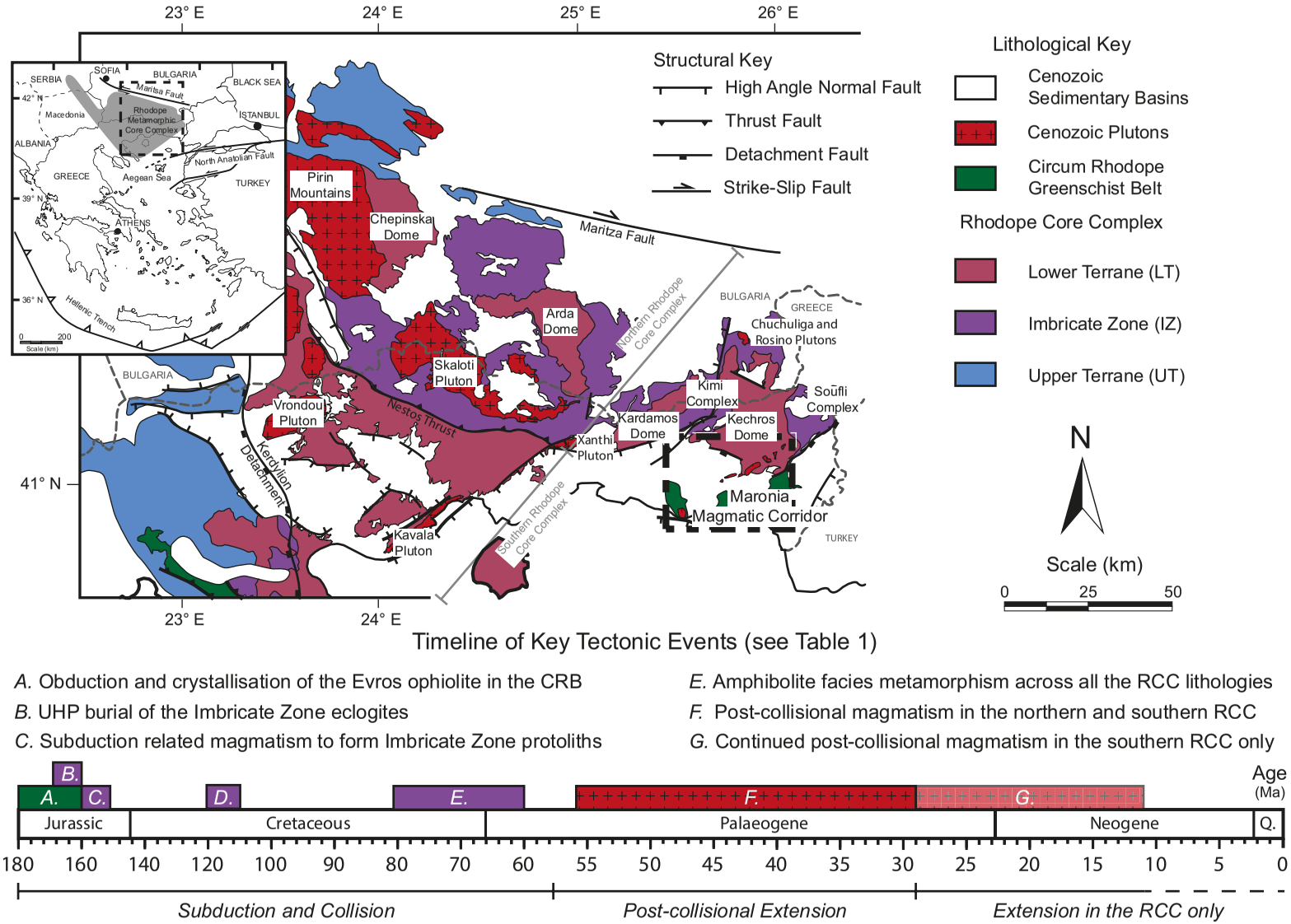

Figure 1. Geological map and geochronological timeline of the Rhodope Massif (inset gray-colored area from Bonev et al., 2013); geological map modified from Burg (2011) and Kydonakis et al. (2014), and timeline complied from Burg (2011). The northern Rhodope Core Complex (RCC) is separated from the southern RCC by the Nestos Thrust, as marked by the gray line. Within the northern RCC, domes of lower plate gneiss were exhumed along multiple detachment and thrust faults, which are poorly mapped and not marked on the map. The exception is the Kechros Detachment, local to the Maronia Magmatic Corridor (the study area) and is marked where field and ASTER data suggest the presence of a significant trans-crustal structure. Four gneiss domes make up the northern RCC; from west to east they are the Chepinska, Arda, Kardamos–Kesebir, and Biala-Rika–Kechros domes. The timeline summarizes the key tectonic events that affected the RCC from subduction through to continent collision and exhumation (using literature geochronology compiled in Table 1; Wawrzenitz and Mposkos, 1997; Liati et al., 2002; Bauer et al., 2007; Cornelius, 2008; Meinhold et al., 2010; Bonev et al., 2013, 2015). A compilation of geochronological data from each of the Cenozoic plutons marked can be found in Table 2 (Meyer, 1968; Dürr et al., 1978; Kokkinakis, 1980; Zagorchev et al., 1987; Del Moro et al., 1988; De Wet et al., 1989; Liati and Kreuzer, 1990; Gilg and Frei, 1994; Dinter et al., 1995; Frei, 1996; Christofides et al., 2000; Eleftheriadis et al., 2001; Ovtcharova et al., 2004; von Quandt and Petycheva, 2005; Marchev et al., 2006, 2013; Soldatos et al., 2008; Jahn-Awe et al., 2010; Georgiev et al., 2013; Rohrmeier et al., 2013). Following exhumation, the northern RCC underwent NE-oriented extension, accommodated by a series of N- to NNE-trending high-angle normal faults and E-trending dextral strike-slip faults.

TABLE 1. COMPILATION OF LITERATURE GEOCHRONOLOGY OF RELEVANT GEOLOGICAL EVENTS IN THE KECHROS DOME AND SURROUNDING TERRANES OF THE NORTHERN RHODOPE CORE COMPLEX

Geological event	Location	Age (Ma)	Method	Reference
Circum Rhodope Belt Ophiolite Gabbro Crystallization	Evros Ophiolite	176.4 ± 0.93 163.5 ± 3.85	U-Pb zircon LA-ICP-MS	Bonev et al., 2015
Circum Rhodope Belt Protolith Formation	Maronia–Makri Block	320–280 240	U-Pb zircon SHRIMP	Meinhold et al., 2010
Imbricate Zone Crustal Melting	Kimi Complex	61.9 ± 1.9	U-Pb zircon SHRIMP	Liati et al., 2002
Imbricate Zone Metamorphic Events	Kimi Complex	79 ± 3	U-Pb zircon SHRIMP	Bauer et al., 2007
	Kimi Complex	73.5 ± 3.4	U-Pb zircon SHRIMP	Liati et al., 2002
	Kimi Complex	119 ± 3.5	Sm-Nd WR-GRT-CPX	Wawrenitz & Mposkos, 1997
	Kimi Complex	115	U-Pb zircon SHRIMP	Bauer et al., 2007
	Kimi Complex	160–170	U-Pb zircon SHRIMP	Bauer et al., 2007
Imbricate Zone Protolith Formation	Kimi Complex	117.4 ± 1.9	U-Pb zircon SHRIMP	Liati et al., 2002
	Soufli Complex	154 ± 1.5	U-Pb zircon LA-ICP-MS	Bonev et al., 2015
	Kimi Complex	150–160	U-Pb zircon LA-ICP-MS	Cornelius 2008
	Soufli Complex	160 ± 0.69	U-Pb zircon LA-ICP-MS	Bonev et al., 2015
	Kimi Complex	290–310	U-Pb zircon LA-ICP-MS	Cornelius 2008
	Kimi Complex	288 ± 6	U-Pb zircon SHRIMP	Bauer et al., 2007
Pangaion (/Thracia/Drama) Terrane Protolith Formation	Kechros Dome	250–330	U-Pb zircon LA-ICP-MS	Cornelius 2008
	Kechros Dome	410–480	U-Pb zircon LA-ICP-MS	
	Kechros Dome	ca. 455	U-Pb zircon LA-ICP-MS	Bonev et al., 2013
	Kechros Dome	528–534	U-Pb zircon LA-ICP-MS	

Note: Compiled from Bonev et al. (2015). LA-ICP-MS—laser ablation inductively coupled plasma–mass spectrometry; WR-GRT-CPX—whole-rock-garnet-clinopyroxene; SHRIMP—sensitive high-resolution ion microprobe.

convergence to subduction-related slab rollback and trans-crustal extension (Burchfiel et al., 2008).

Trans-Crustal Extension and Core Complex Exhumation

The Rhodope Massif was exhumed during late Cretaceous–Cenozoic trans-crustal extension driven by Aegean slab rollback (e.g., Jolivet and Brun, 2010; Ring et al., 2010). Paleocene–Oligocene localized extension formed a series of gneiss domes across the northern RCC and initiated exhumation along the Kerdyllion Detachment in the southern RCC (e.g., van Hinsbergen et al., 2008; Kydonakis et al., 2014, 2015). Dehydration partial melting during core complex unroofing and exhumation is recorded in temporally sporadic Paleocene–Eocene pegmatites and leucogranites across both the northern RCC and southern RCC (e.g., Del Moro et al., 1990; Mposkos and Wawrzenitz, 1995; Wawrzenitz and Krohe, 1998; Lips et al., 2000; Liati et al., 2002). Maastrichtian–Paleocene to early Eocene sediments unconformably overlie the gneiss domes of the northern RCC, indicating that these domes must have been exhumed, at least in part, before the early Eocene (Boyanov et al., 1982; Burg, 2011).

Exhumation in the northern RCC ceased abruptly in the Oligocene, likely with the onset of post-collisional volcanism across the northern RCC (e.g., Rohrmeier et al., 2013), and resulted in an E-trending belt of small (~30 km diameter), unconnected gneiss domes (Kydonakis et al., 2015). This was contemporaneous with a change in extension style across the Aegean. Early Eocene–Oligocene extension was localized in the northern Aegean, restricted to the northern limit of the hinterland, the northern and southern RCC (Kydonakis et al., 2015). From the mid-Miocene onward, extension was distributed across the Aegean with the formation of the Central Cyclades Core Complex further south and continued exhumation and SW-rotation of the southern RCC (van Hinsbergen et al., 2008; Kydonakis et al., 2014, 2015). The change in extension style is attributed to an acceleration in trench retreat related to the increased rate of convergence between Africa and Eurasia and slab tearing beneath western Turkey in the mid-Miocene (e.g., Jolivet and Brun, 2010; Jolivet et al., 2013; Brun et al., 2016).

Post-subduction magmatism was contemporaneous with trans-crustal extension, punctuating across the Rhodope Massif from the middle Eocene (42 Ma, Smiliyan and Yugovo Plutons; Table 2; Rohrmeier et al., 2013) to the mid-Miocene (11.32 Ma, Strymon Valley volcanics; Table 2; Georgiev et al., 2013). Post-subduction magmatism is closely linked to extension, with trans-crustal structures providing pathways for magmas, evidenced by the spatial association of plutonic rocks and detachment fault systems (e.g., Jones et al., 1992; Pe-Piper and Piper, 2006; Fig. 1). This is noticeable in the distinction between the northern RCC and southern RCC, where magmatism and concurrent volcanism cease in the late Oligocene in the northern RCC (e.g., Márton et al., 2010; Marchev et al., 2010) but continue into the Miocene in the southern RCC (Table 2; Georgiev et al., 2013).

Unconformably overlying the northern RCC metamorphic basement, syn-extensional sedimentation started in the mid-late Eocene as a transgressive sequence of conglomerates, limestones, sandstones, and marls filled the Thrace supra-detachment basin, formed in accommodation space to the SE of the exhuming northern RCC (Kilias et al., 2013). The switch from trans-crustal, ductile extension to upper-crustal, brittle extension in the northern RCC is recorded by the change in depositional environment from a supra-detachment basin in the Eocene-Oligogene, to a series of cross-cutting N-S– to NNE-SSW–trending fault-bound basins in the Oligocene-Miocene (Burchfield et al., 2003, 2008; Kilias et al., 2013).

The Maronia Magmatic Corridor

The MMC is a NE-trending magmatic belt, comprising at least six Oligocene gabbroic to granodioritic intrusions (Fig. 2): the Tris Visses, Halasmata, Leptokaria, Kirki, Kassiteres, and Maronia plutons. The MMC is hosted in the easternmost dome of the northern RCC, the Biala-Rika-Kechros dome (from here onward referred to as the Kechros Dome). First described by Del Moro et al. (1988), the MMC plutons all intrude the northern RCC and associated lithologies, hosted either within the Kechros gneiss dome to the NE (Halasmata and Tris Visses), straddling the Kechros basal detachment in the center of the corridor (Leptokaria),

TABLE 2: COMPILATION OF EXISTING LITERATURE GEOCHRONOLOGY OF THE POST-COLLISIONAL INTRUSIONS OF THE RHODOPE MASSIF

Intrusion	Emplacement age (Ma)	Uncertainty (2 sigma)	Method	Reference
Northern Rhodope Core Complex				
Rila	66.8	± 0.3	U-Pb zircon (TIMS)	von Quadt and Peytcheva, 2005
	69.3	± 0.3		
Central Pirin/Spanchevo	37	± 2	Rb-Sr whole rock	Zagorcev et al., 1987
	56	± 0.5	U-Pb zircon (LA-ICP-MS)	Jahn-Awe et al., 2010
Smiliyan	41.92	± 0.22	U-Pb zircon (TIMS)	Kasier-Rohrmeier et al., 2013
	43.4	± 1.41	U-Pb zircon	Ovtcharova et al., 2004
Teshovo	32	± 0.02	U-Pb zircon (LA-ICP-MS)	Jahn-Awe et al., 2010
Skaloti	42-44		40Ar/39Ar feldspar	Soldatos et al., 2008
	49.99	± 0.88	40Ar/39Ar biotite	
	55.93	± 0.28	U-Pb zircon (TIMS)	
Topolovo	52.54	± 0.19	U-Pb zircon (LA-ICP-MS)	Marchev et al., 2013
Chuchuliga	68.94	± 0.40	U-Pb zircon (TIMS)	Marchev et al., 2006
Rosino	68	± 15	U-Pb zircon (TIMS)	Marchev et al., 2006
MMC	28.4	± 0.9	Rb-Sr biotite	Del Moro et al., 1988
	34.9	± 1.5		
Yugovo	42.29	± 0.08	U-Pb zircon (TIMS)	Kasier-Rohrmeier et al., 2013
	42.3	± 0.54	U-Pb zircon (TIMS)	Ovtcharova et al., 2004
Drangovo	49.9	± 0.21	U-Pb zircon (LA-ICP-MS)	Marchev et al., 2013
Dolno Dryanovo	55	± 0.5	U-Pb zircon (LA-ICP-MS)	Jahn-Awe et al., 2010
Southern Rhodope Core Complex				
Xanthi	27.1	± 0.4	K-Ar biotite	Meyer, 1968
	27.9	± 0.5		
	30	± 1	K-Ar hornblende	Liati & Kreuzer, 1990
Vrondou	30	± 3	K-Ar biotite	Dürr et al., 1978
Kavala	15.5	± 0.5	K-Ar biotite	Kokkinakis, 1980
	17.8	± 0.8		
	21.1	± 0.8	U-Pb titanite	Dinter et al., 1995
Ouranopolis	47	± 0.7	Ar-Ar muscovite	De Wet et al., 1989
Stratoni	19.7	± 0.6	K-Ar biotite	Gilg and Frei, 1994
	26.9	± 2.0	U-Pb zircon (TIMS)	
	27.9	± 1.2	U-Pb zircon (TIMS)	
	19.2	± 0.2	U-Pb zircon (LA-ICP-MS)	Siron et al., 2016
	25.4	± 0.2		
Skouries	20.6	± 0.5	U-Pb zircon (LA-ICP-MS)	Siron et al., 2016
Mesoropi	13.8	± 0.5	Ar/Ar biotite	Eleftheriadis et al., 2001
	21.7	± 0.5	Ar/Ar muscovite	
Ierissos	53.6	± 6.2	U-Pb uranothorite (TIMS)	Frei, 1996
Strymon Valley	11.32	± 0.099	U-Pb zircon (TIMS)	Georgiev et al., 2013
	12.235	± 0.026	U-Pb zircon (LA-ICP-MS)	
Samothraki	18	± 0.2	Rb-Sr biotite	Christofides et al., 2000
	18.5	± 0.2		

Note: From Burg (2011), supplemented by more recent geochronology. TIMS—thermal ionization mass spectrometry; LA-ICP-MS—laser ablation-inductively coupled plasma–mass spectrometry.

or within the CRB greenschist basement to the SW (Kirki, Kassiteres, and Maronia; Fig. 2). Later Oligocene intercalated sedimentary and volcanic units onlap onto the MMC intrusions. Both the Kassiteres and Maronia plutons are cross-cut by younger porphyritic microgranite intrusions and host occurrences of porphyry–epithermal-style Au-Mo-Cu mineralization (e.g., Melfos et al., 2002; Voudouris et al., 2006). Rb-Sr biotite–whole-rock isochron dating by Del Moro et al. (1988) suggests that the MMC plutons were emplaced between ca. 32 and 28 Ma, younging progressively from NE to SW along the belt.

METHODS

Field Geology and Petrology

Field observations, with particular focus on relationships between lithologies, were made over multiple summer field seasons in northeastern Greece. We have prepared our geological map, Figure 2, from existing geological maps of the area supplemented by our own field observations. The spatial extent of the plutons, in particular Kirki, Leptokaria, Halasmata, and Tris Visses, are poorly constrained due to difficult field conditions. The lack of exposure, steep topography, dense vegetation, and poor road access bias the outcrop localities of both this work and previous geological mapping by Del Moro et al. (1988), with most mapped outcrops found along small river channels. However, based on our field observations, we consider it more likely that the observed plutons represent small outcrops of a larger magmatic system interconnected at depth that is poorly exposed, and that additional outcrops could be found in more inaccessible areas.

A suite of 36 samples was collected from the MMC, representing each of the observed intrusive lithologies and alteration styles. At least eight samples were taken from each of the Maronia and Kassiteres plutons, and from across the Kirki–Leptokaria–Halasmata–Tris Visses outcrops to reflect changes in mineralogy between samples. Standard polished thin sections and epoxy mounts were prepared for a representative selection of samples from each pluton, and detailed petrographic observations were

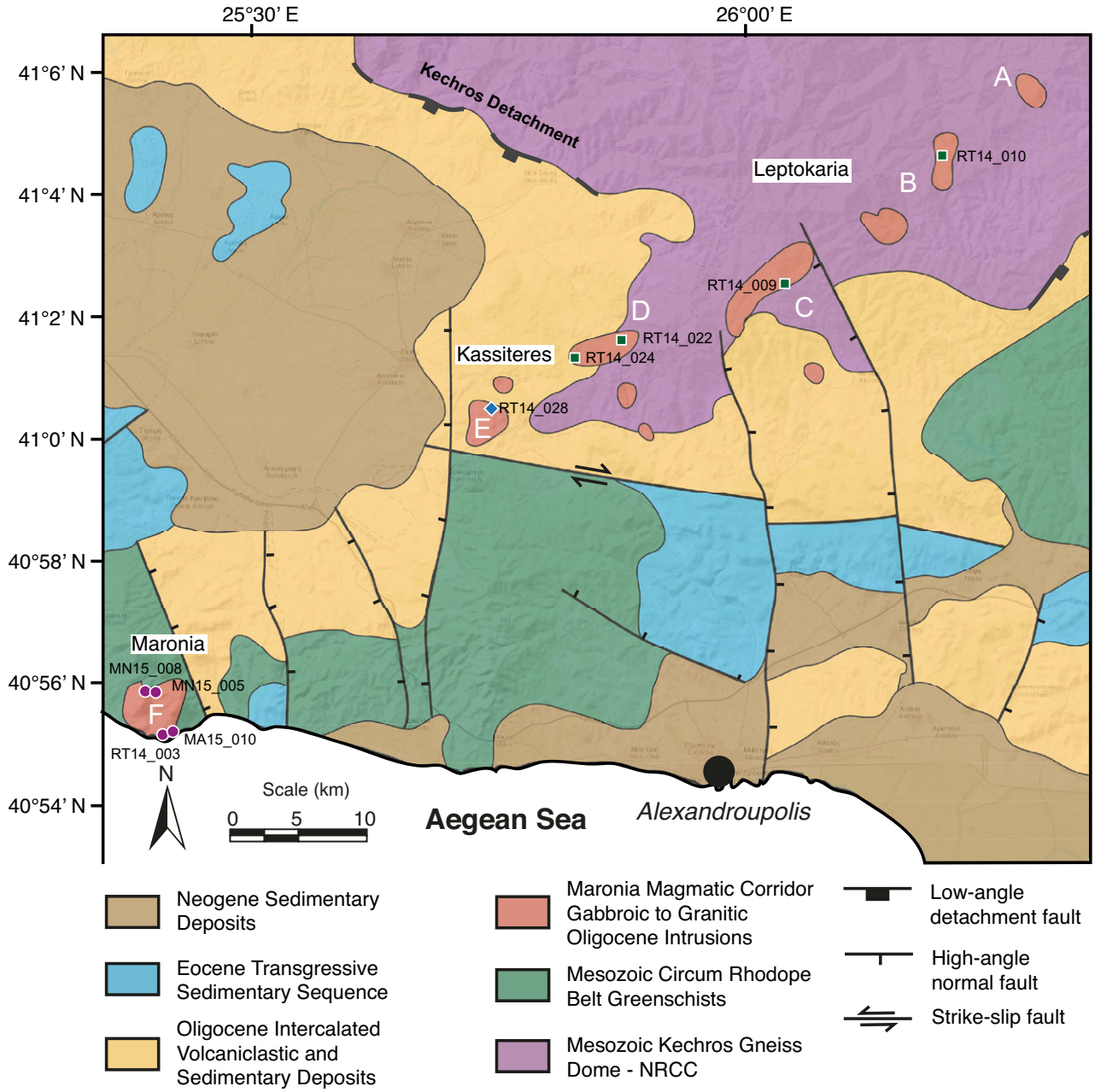

Figure 2. A geological map of the Maronia Magmatic Corridor and surrounding area drawn from field observations, interpretations of the digital elevation model (DEM), and adaption of the existing maps of Del Moro et al. (1988), and Bornovas and Rondogianni-Tsiabaou (1983). The white letters refer to the pluton names of Del Moro et al. (1988): A—Tris Visses; B—Halasmata; C—Leptokaria; D—Kirki; E—Kassiteres; F—Maronia. The symbols show the location of the named samples used for high-precision U-Pb geochronology: squares—Leptokaria; diamond—Kassiteres; circles—Maronia. The Oligocene volcaniclastic and sedimentary units onlap onto the Kechros Dome, and the basal detachment is not exposed; field evidence of a trans-crustal extensional structure is observed in pegmatite dykes close to the margin of the dome and top to the SW microstructures (Kydonakis et al., 2014).

made under both transmitted and reflected light. Point counting of the least altered thin section(s) of each of the plutons was undertaken to obtain representative modal compositions of the samples. Scanning Electron Microscope (SEM) analysis was undertaken at the University of Bristol on a Hitachi S-3500 N instrument with 20 kV accelerating voltage and a 15 mm working distance. Phase identification was performed using energy dispersive spectra (EDS), and back-scatter electron (BSE) imagery was used to establish key textural relationships.

Analytical Methods

Whole-Rock Geochemistry

Powders of <25 µm grain size were prepared at the University of Bristol and analyzed in the Inorganic Geochemical Laboratories at the British Geological Survey (BGS), Keyworth. Powders were prepared for each of the igneous lithologies collected, with a total of 36 samples and eight repeats analyzed. Weathered outer rims of individual samples were

removed such that only the freshest material from the cores of the samples were used for analysis. Samples were then crushed and milled in a ball mill using an agate jar with 12 agate balls. Due to the large grain size (>1 mm) and relative heterogeneity of the samples, >1 kg of rock was used to ensure a homogenous powder was produced; a greater weight of sample was used for coarser-grained samples from the Maronia pluton. Samples were analyzed following the UKAS Accreditation Schedule using wavelength dispersive–X-ray fluorescence spectrometry (WD-XRFS) on fused glass beads for major and minor element oxides, Na_2O_2 fusion inductively coupled plasma–mass spectrometry (ICP-MS) for minor and trace element concentrations, and an aqua regia digest ICP-MS for Sc and Te.

New geochemical data presented in this study supplements previously published work by Del Moro et al. (1988), Papadopoulou et al. (2004), and Mavroudchiev et al. (1993), presenting for the first time a complete suite of trace element and REE analyses for the entire magmatic belt. The results have been filtered by loss on ignition (LOI) values such that any results with LOI >2 wt% have been omitted, removing any bias in the results from heavily clay-altered or hydrated samples.

U-Pb Zircon Geochronology

A subset of nine samples from the MMC sample suite were selected for high-precision U-Pb zircon geochronology (Maronia, $n = 4$; Kassiteres and Leptokaria $n = 5$). The MMC zircons have broadly similar euhedral morphologies with many inclusions of apatite, titanite, and melt. Zircons from Maronia were typically larger than those from Kassiteres and Leptokaria and were less abundant in the mineral separate. Inclusion- and defect-free crystals with well-preserved euhedral crystal faces were preferentially selected from the mineral separate for analysis (further details of sample preparation and zircon selection are included in GSA Data Repository File DR2[1]). The remaining zircon crystals were mounted in epoxy, polished, and imaged at the University of Bristol using a Centaur Cathodoluminescence (CL) detector on a Hitachi S-3500N Scanning Electron Microscope at 10 kV and 23 mm working distance. CL imagery of the zircons was used to investigate the internal morphology of the crystals, with particular focus on growth and resorption features in the zircons.

A total of 42 zircon crystals were analyzed at the NERC Isotope Geosciences Laboratory (NIGL) using the CA-ID-TIMS technique. Three to seven individual zircon crystals from each sample were thermally annealed and chemically abraded to reduce Pb loss (Mattinson, 2005). Isotope dilution and mass spectrometry protocol followed the techniques and instrumentation described by Sahy et al. (2015), and further details are included in GSA Data Repository File DR2.

FIELD GEOLOGY AND PETROLOGY

We present primary field and petrographic observations of the MMC plutons. This work builds upon that of previous authors, in particular Del Moro et al. (1988), and focuses on the most voluminous intrusions along the belt: Maronia, Kassiteres, and Leptokaria (Fig. 2). Two additional, later phases of magmatism are found intruding each of the plutons: an array of aplitic dykes and small (~500 m^2), silicic porphyry intrusions. The felsic units are volumetrically insignificant compared to the host plutons and associated with post-pluton hydrothermal activity, including porphyry-style alteration and mineralization in the area, leading to intense alteration of these rocks (e.g., Melfos and Voudouris, 2016, and references therein). We consider the small-volume, evolved lithologies to be less important to the discussion on the changing geochemistry of the mantle magmatic system in the northern RCC, as they are highly fractionated and likely represent a mixed geochemical signature, reflecting both crustal and mantle melt sources.

The Leptokaria Complex

The Leptokaria, Kirki, Halasmata, and Tris Visses plutons were first described individually by Del Moro et al. (1988). However, in this paper, we group these plutons together on the basis of similar geochemistry and age, and we refer to them collectively as the Leptokaria complex, after the largest pluton in the group (Fig. 2).

The equigranular (0.2–1.0 mm) Leptokaria complex ranges from monzogabbro to granite in composition (Fig. 3A). A primary assemblage of phenocrystic plagioclase + magnetite + hornblende + biotite is found in all samples of the Leptokaria pluton; clino- and ortho-pyroxene are present in the dioritic Leptokaria samples, while quartz + K-feldspar and accessory zircon + apatite are also present in the more evolved samples. Interstitial, granophyric quartz and K-feldspar intergrowths are found throughout the more evolved samples. Weak alteration, principally chlorite + epidote ± biotite ± orthoclase, is pervasive across Leptokaria, with breakdown of mafic phases and sericitization of plagioclase. Small (0.5–1-cm-wide) veinlets of albite ± chlorite ± epidote are also common. Five of the Leptokaria samples have a cumulate-like texture with interlocking phenocrysts of plagioclase, amphibole (replacing relict clinopyroxene), and magnetite and the development of interstitial, poikolitic amphibole and plagioclase and visible plagioclase rims (Figs. 3B–3C). These cumulate-like rocks likely characterize the mineral phases present during earliest magmatic crystallization and differentiation. Alteration is continuous through the cumulate samples with chlorite-biotite-epidote alteration of mafic phases the most common reactions observed.

The Leptokaria plutons are intruded into ortho- and para-gneisses of the Kechros Dome within the northern RCC. Around Leptokaria village, the pluton is hosted in a two-mica pegmatitic leucogranite, although the contact between the leucogranite and Leptokaria complex is not seen. Contacts between the plutons and the gneisses elsewhere in the Leptokaria Complex are undulose, with mixing of globules of gneiss in the pluton and vice-versa, this suggests that the host gneisses were not completely solid during magma emplacement and accumulation.

Kassiteres

Kassiteres is a medium-grained (1–3 mm), clinopyroxene-hornblende diorite and is the next pluton moving SW along the MMC from Leptokaria (Fig. 2). The smallest of the named intrusions, Kassiteres has an aerial extent of ca. 1.8 km^2. Kassiteres intrudes into metapelitic greenschists of the CRB basement and is unconformably overlain by Oligocene volcaniclastic units. The primary mineralogy of the Kassiteres diorite is clinopyroxene + hornblende + plagioclase + biotite + magnetite phenocrysts and interstitial K-feldspar + quartz with accessory apatite + titanite + zircon (Fig. 3E). Mixing of mafic, clinopyroxene-rich, and felsic, biotite-rich, end members are visible on the macroscopic scale, suggesting periodic injection of new melt into the crystallizing magmatic system (Fig. 3D). Interstitial granophyric quartz-feldspar intergrowths suggest rapid cooling of interstitial melt during the later stages of pluton crystallization (Fig. 3F).

The Kassiteres pluton is variably altered due to hydrothermal activity related to the later intrusion of a porphyritic stock and aplite dykes. Breakdown of clinopyroxene and hornblende to biotite, chlorite, and plagioclase is characteristic of potassic alteration at Kassiteres, pervasive to varying

[1]GSA Data Repository Item 2018177, full whole-rock geochemical analyses, detailed U-Pb isotope results, and supplementary material with full analytical methods, is available at http://www.geosociety.org/datarepository/2018, or on request from editing@geosociety.org.

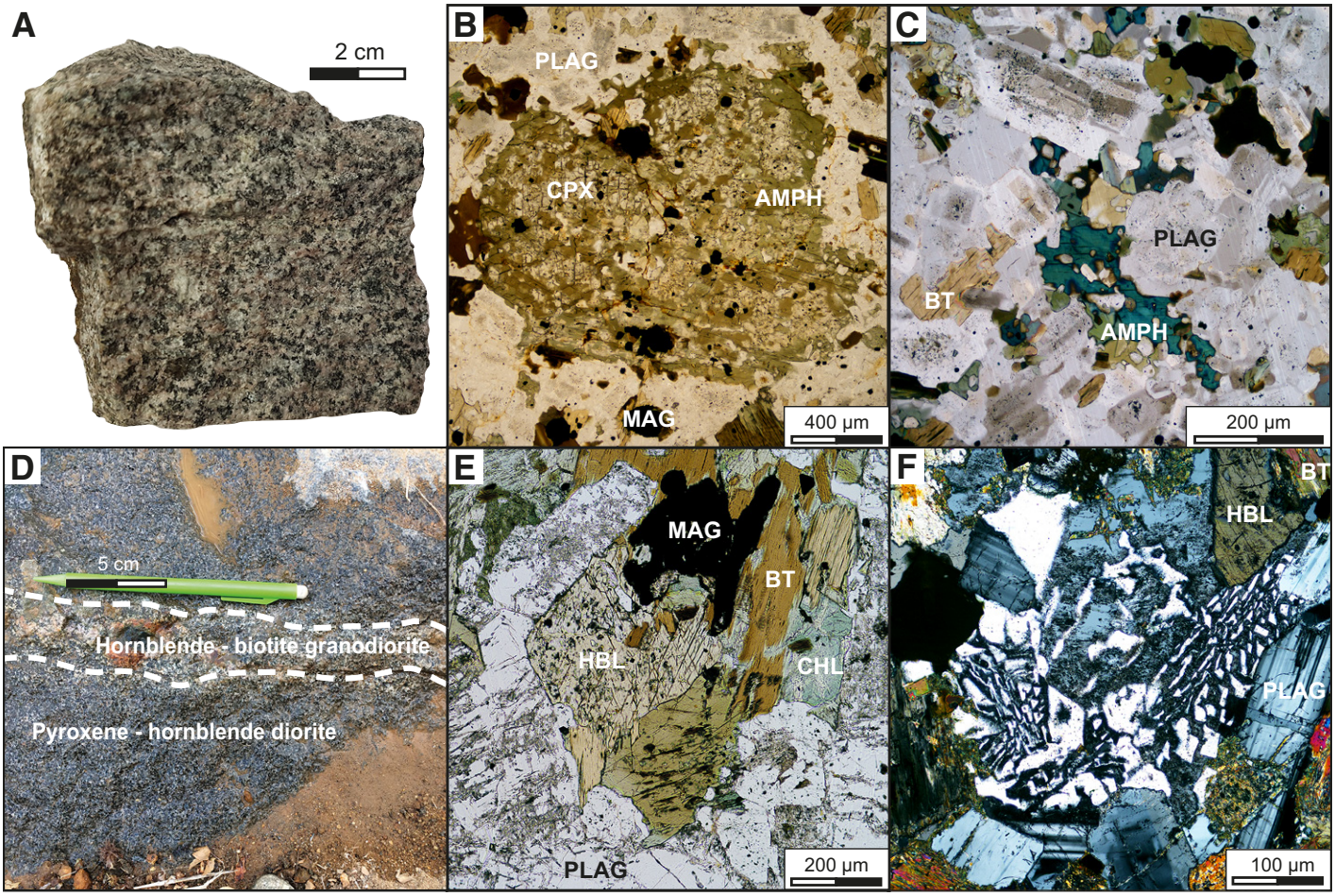

Figure 3. Representative field photos and photomicrographs of the Kassiteres and Leptokaria samples. PLAG—plagioclase; MAG—magnetite; AMPH—amphibole; CPX—clinopyroxene; BT—biotite; CHL—chlorite; HBL—hornblende. (A) A granitic sample from the Leptokaria suite. (B) Photomicrograph of the Leptokaria cumulate where a relict clinopyroxene phenocryst has been almost completely replaced by amphibole. (C) Photomicrograph of the interlocking plagioclase phenocrysts with clear rim growth surrounded by interstitial poikilitic amphibole. (D) Magma mixing of clinopyroxene-hornblende and hornblende-biotite–rich end members of the Kassiteres intrusion. (E) A photomicrograph of the Kassiteres intrusion with primary hornblende + biotite + magnetite + plagioclase and minor chloritic alteration. (F) A photomicrograph of granophyric quartz-feldspar intergrowths from Kassiteres, also observed in the Leptokaria suite.

degrees of intensity throughout the pluton. Advanced clay alteration is found in discrete fault zones within the diorite where the fault planes provide a pathway for enhanced fluid-wallrock interaction. This alteration grades from silicified, advanced argillic alteration (silica + low-temperature clays) proximal to the fault plane, to argillic alteration (high-temperature clays) over 5 m from the fault. A diffuse gradation into potassically altered diorite occurs over a greater distance of 15–20 m from the faults.

Maronia

Maronia is the southernmost pluton of the MMC, separated by ~30 km from its nearest neighbor, Kassiteres. Outcropping as a stock with an area of ~3.2 km^2, it is intruded into metapelites and marbles of the CRB. Three intrusive lithologies were recognized at Maronia by Papadopoulou et al. (2004): a voluminous monzonite–quartz monzonite unit (Fig. 4A), a minor gabbroic unit, and a minor porphyritic granitic unit. The gabbro is texturally and mineralogically indistinguishable from the monzonite–quartz monzonite unit in all but whole-rock geochemistry, while the granite porphyry shows sharp, cross-cutting contacts with the rest of the pluton (Fig. 4F). In this paper, we consider the gabbro–monzonite–quartz monzonite as a single unit (referred to herein as the monzonite unit) with subdivisions arising from varying phenocryst proportions.

The primary mineralogy of the monzonite is clinopyroxene + orthopyroxene + amphibole (tremolite-ferrosillite) + biotite + plagioclase + K-feldspar + apatite + magnetite + quartz ± rare olivine with accessory zircon. 1–2-cm-diameter phenocrysts of primary plagioclase (50%–80% by area), clinopyroxene (5%–15%), and minor orthopyroxene (1%–3%) are surrounded by interstitial K-feldspar (up to 20%; Fig. 4C). Primary biotite and amphibole phenocrysts in textural equilibrium with adjacent crystals are very rare and are more commonly found as secondary breakdown rims of primary pyroxene phenocrysts (Fig. 4B). Evidence of post-magmatic hydrothermal alteration is visible in minor sericitization and uralization of plagioclase and pyroxene-amphibole phenocrysts respectively.

Additional igneous facies are observed along the western margin of Maronia where the pluton intrudes CRB marbles. In addition to a thin (~1 m) endo-skarn boundary along the marble-monzonite contact (Katerinopoulou et al., 2009; Fig. 4E), an orthocumulus facies is exposed in

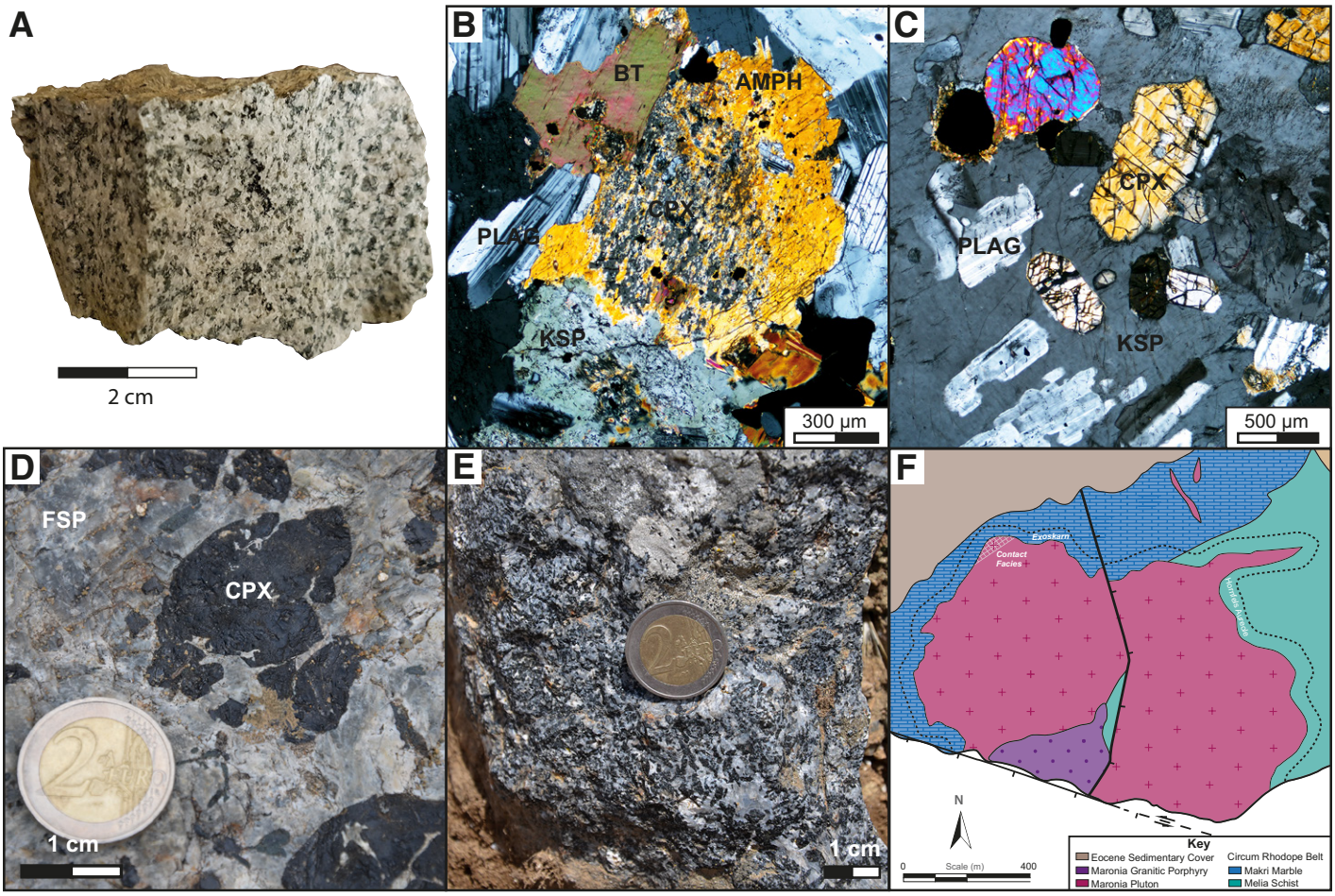

Figure 4. Field evidence from the Maronia pluton. AMPH—amphibole; BT—biotite; CPX—clinopyroxene; KSP—anorthite-albite; PLAG—orthoclase-albite. (A) Representative hand sample of the equigranular, coarse-grained (1–2 mm) Maronia monzonite. (B) Crossed-polar photomicrograph of a primary augite phenocryst with a breakdown rim of tremolite-ferrosilite amphibole. (C) The typical poikilitic texture of the monzonite with clinopyroxene and olivine adacrysts and oikocrystic anorthite. (D) Field photo of the Maronia contact facies with 2 cm phenocrysts of augite in K-feldspar phenocrysts up to 10 cm in diameter. (E) Endoskarn field photo. (F) Geological map of the Maronia pluton drawn from field observations and modified from Melfos et al. (2002).

the northwest of the pluton extending for up to 10 m into the monzonite from endoskarn boundary (Fig. 4D). Cumulus pyroxene adacrysts and intercumulus oikocrystic orthoclase-albite suggest that the western margin of the pluton exposes close to the base of the Maronia plutonic system. This orthocumulus facies is not observed on the eastern margin of Maronia where a ~250-m-wide hornfels aureole extends into the host CRB metapelites.

The NNE-SSW trending Ktismata Fault cuts the pluton separating the eastern and western portions of the pluton (Melfos et al., 2002; Fig. 4F). Differing intrusive relationships between the western (deeper, orthocumulus facies) and eastern (shallow, baked aureole) margins of the pluton suggest an east-dipping normal fault. Minimal right-lateral displacement of < 100 m is observed where the fault cuts the northern pluton margin, which can be accounted for by a minor oblique component of motion. An additional strike-slip fault, the Marmaritsa Fault, cuts the southern margin of the Maronia pluton subparallel to the coastline. This structure is part of a regional crustal trend, potentially related to the North Anatolian Fault Zone (Melfos et al., 2002). The brittle nature of the faulting, cutting Oligocene magmatic features within Maronia, suggest post-emplacement initiation of both structures.

ANALYTICAL RESULTS

Whole-Rock Geochemistry

The MMC samples vary in composition from 48 to 68 wt% SiO_2 (Fig. 5; Table 3; GSA Data Repository Table DR1). The Maronia pluton has a more restricted SiO_2 compositional range (50–56 wt% SiO_2), while the Kassiteres and Leptokaria samples cover the full range (48–68 wt% SiO_2). Within the Leptokaria sample suite, a difference in SiO_2 content separates cumulate-like samples (48–53 wt% SiO_2) from the intermediate to felsic plutonic samples (55–68 wt% SiO_2), with all the Leptokaria samples falling on a linear fractionation trend. Samples from the MMC follow a calc-alkaline differentiation trend; however, their similarity to "typical" calc-alkaline magmatism is limited. As SiO_2 increases with differentiation, compatible elements, including MgO, $Fe_2O_3^T$, TiO_2, and CaO (Figs. 6B–6E), decrease. A highly scattered, negative correlation between Al_2O_3 and SiO_2 is observed in all of the MMC samples (Fig. 6A). The incompatible elements, e.g., Na_2O, K_2O and Ba (Figs. 6F–6G), show a positive correlation, increasing with SiO_2. Sr behaves as a compatible element in all the MMC samples with a steady decrease in Sr

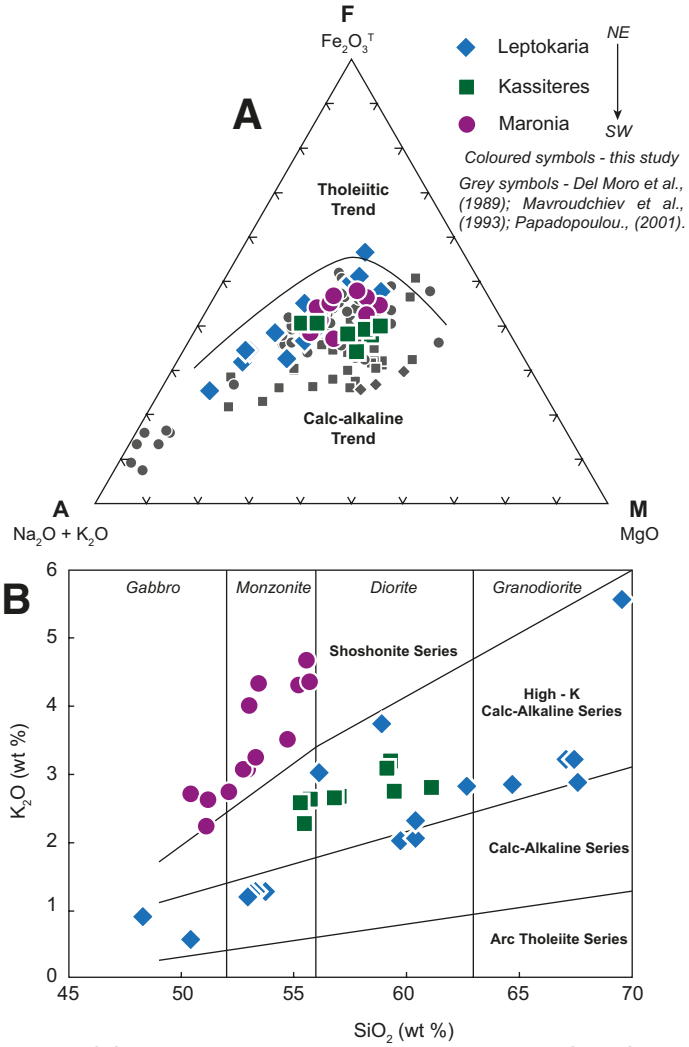

Figure 5. (A) AFM plot of the Maronia Magmatic Corridor (MMC) suite after Irvine and Baragar (1971); the samples plot on a calc-alkaline trend but vary to higher MgO fractions than would typically be expected. (B) A K_2O versus SiO_2 plot with rock-type classification after Peccerillo and Taylor (1976). The MMC samples range from 47–70 wt% SiO_2 (this study) with a more restricted range of compositions, 51–56 wt% SiO_2 at Maronia. Samples of the Leptokaria cumulate can be distinguished from the main Leptokaria trend from 48 to 54 wt% SiO_2 and have the lowest alkali component. The Maronia suite can be clearly distinguished from the Kassiteres and Leptokaria samples by elevated K_2O, falling along a shoshonitic trend, while the Kassiteres and Leptokaria are moderately potassic on a high-K calc-alkaline trend.

with fractionation (Fig. 6H). The MMC shows a spatial and geochemical migration from purely calc-alkaline magmatism in the Leptokaria samples in the north, to high-K calc alkaline magmatism in the central Kassiteres samples, to shoshonitic magmatism in the southern Maronia pluton (Fig. 5A). In the Maronia samples, the absolute concentration of the incompatible elements is 1–1.5 times greater than in Kassiteres and Leptokaria samples, in line with shoshonitic magmatism (Figs. 6G–6H).

Irregular trace element patterns are observed from all plutons along the MMC (Fig. 7A). The MMC samples are enriched in fluid mobile, large-ion lithophile elements (LILEs; e.g., Ba, Rb, Pb) and depleted in fluid immobile, high field-strength elements (HFSEs; e.g., Nb, Ta, Zr) compared to the primitive mantle, in a trace signature typical of a metasomatized, fertile mantle source (Elliott et al., 1997). The plutons are enriched in the light REEs relative the heavy REEs (Fig. 7B) and show decreasing Dy/Yb (middle REE to heavy REE fractionation) with differentiation (Fig. 6J). The mildly concave REE pattern is flatter than the highly convex, amphibole-controlled REE fractionation trend, and is most similar to that of a clinopyroxene-hornblende–controlled REE pattern (Pearce and Peate, 1995; Tatsumi, 1989; Davidson et al., 2013). A pronounced, negative Eu anomaly, which decreases with increasing SiO_2, is observed in all of the MMC samples (Fig. 6I).

U-Pb Zircon Geochronology

CL imaging revealed simple zoning patterns in most all of the zircons from the MMC (further descriptions are included in GSA Data Repository File DR2). Oscillatory and sector zoning in the crystals reflects a simple magmatic history of the zircons with little evidence of zircon inheritance suggesting the zircons experienced a single period of crystallization. Therefore, dissolution of full zircon crystals was justified to use the largest sample volume and reduce analytical uncertainty, offering the highest-precision dates. Two individual zircon analyses were excluded from our interpretations as high common Pb (Pb* > 2.5 pg) was taken as an indicator of a low precision analysis (see GSA Data Repository Table DR3).

Our results were interpreted within a magmatic framework in which it is recognized that zircon crystallization is protracted over time scales of 10^5–10^6 yr (e.g., von Quadt et al., 2011). The youngest statistically significant population of zircons was sought to represent the timing of the final stages of crystallization. Our preferred age interpretations are presented in Table 4; alternative interpretations and a discussion of the sample discordance are included in GSA Data Repository File DR2. All ages reported are $^{206}Pb/^{238}U$ to minimize the influence of excess ^{207}Pb, the result of initial U/Pa disequilibrium, on our age interpretations (Crowley et al., 2007). Dates are reported in millions of years ago (Ma) to 2σ uncertainty.

The $^{206}Pb/^{238}U$ ages form two distinct groups (Fig. 8). We can interpret two geological windows in time for pluton emplacement and crystallization, (a) intrusion of the Kassiteres and Leptokaria plutons over 0.9 Myrs (from 32.96 to 32.02 Ma); and 2.2 Myrs later (b) intrusion of the Maronia pluton over 0.2 Myrs (from 29.78 to 29.57 Ma). Antecrystic zircons, those crystallized prior to final pluton crystallization either during an earlier phase of magmatism or deeper in the magmatic plumbing system, are recognized in the MMC analyses (e.g., z2 RT14_022; Table DR3 [see footnote 1]). Zircons that are much older that the interpreted ages of crystallization (>5 Myrs) are interpreted as xenocrystic zircons, entrained from the wallrock during magma ascent (e.g., z2 RT14_024; File DR2 [see footnote 1]). The autocrystic zircons, those crystallized in situ in the magmatic system, show good clustering in seven of the nine samples from the MMC, allowing interpretation of a youngest population of zircons (Table 4). In Leptokaria samples RT14_022 and RT14_024, the youngest zircon is taken as a maximum age of crystallization of the pluton, allowing the possibility of younger zircons in the sample.

DISCUSSION

Our geochemical and isotopic data strongly suggest heterogeneity between Maronia and the remainder of the MMC. Therefore, the petrogenesis of the Maronia pluton will be discussed separately to the Kassiteres–Leptokaria magmatic suite before the magmatism along the MMC as a whole is discussed in relation to the extensional tectonics in the Kechros dome.

TABLE 3. ABBREVIATED WHOLE-ROCK GEOCHEMISTRY RESULTS AND MODAL PHASE COMPOSITIONS

	Kassiteres																
Sample identity	KA15-004	KA15-008	KA15-009	KA15-013	KA15-016	KA15-017	RT14-028	LA15-009	LA15-011	LB15-003	LB15-004	LB15-006	LC15-002	LC15-003	LD15-002	LD15-003	RT14-009
SiO_2 (wt%)	55.420	56.860	59.450	61.110	59.100	59.190	55.700	53.790	69.730	50.390	67.630	62.380	60.380	64.730	53.200	52.970	60.240
TiO_2 (wt%)	0.750	0.770	0.740	0.650	0.650	0.700	0.810	0.750	0.390	1.020	0.360	0.620	0.730	0.500	0.840	0.760	0.730
Al_2O_3 (wt%)	14.440	14.870	14.640	15.990	16.090	14.200	15.090	14.650	15.050	19.500	15.630	17.630	17.370	15.970	18.030	19.260	16.390
$Fe_2O_3^T$ (wt%)	7.820	7.380	6.720	6.090	6.670	6.190	7.480	6.850	2.990	8.590	3.580	3.880	6.650	5.160	9.210	8.370	6.230
Mn_3O_4 (wt%)	0.150	0.160	0.100	0.060	0.110	0.110	0.150	0.220	0.070	0.230	0.080	0.110	0.170	0.120	0.190	0.180	0.100
MgO (wt%)	7.050	6.160	5.250	3.100	3.770	6.160	6.810	6.310	1.150	5.680	1.450	2.580	2.730	2.190	4.580	4.130	3.370
CaO (wt%)	7.250	6.280	5.530	5.220	5.320	5.660	7.480	7.510	0.900	9.470	3.870	5.610	5.050	4.300	8.430	8.850	5.910
Na_2O (wt%)	2.530	2.510	2.810	3.180	3.010	2.670	2.820	1.860	2.140	3.070	3.490	4.890	3.120	3.280	2.860	2.980	3.720
K_2O (wt%)	2.270	2.630	2.740	2.780	3.070	3.190	2.590	2.030	5.560	0.550	2.830	0.680	2.300	2.850	1.240	1.180	2.040
P_2O_5 (wt%)	0.240	0.190	0.170	0.140	0.160	0.160	0.190	0.160	0.080	0.230	0.100	0.160	0.170	0.120	0.110	0.150	0.160
LOI	1.640	1.840	1.650	1.460	1.670	1.560	0.870	5.770	1.960	1.210	0.670	1.180	1.300	0.800	0.910	0.810	1.140
Total	99.560	99.650	99.800	99.780	99.620	99.790	99.990	99.900	100.020	99.940	99.690	99.720	99.970	100.020	99.600	99.640	100.030
Rb (ppm)	61.000	54.000	53.000	82.000	77.000	70.000	70.000	48.000	155.000	7.000	79.000	19.000	56.000	76.000	34.000	28.000	43.000
Sr (ppm)	346.000	292.000	298.000	317.000	314.000	259.000	359.000	371.000	258.000	590.000	298.000	562.000	338.000	320.000	385.000	535.000	335.000
Ba (ppm)	1247.000	889.000	783.000	702.000	769.000	793.000	1185.000	759.000	1249.000	227.000	685.000	200.000	670.000	809.000	379.000	404.000	736.000
Eu/Eu*	0.767	0.860	0.674	0.725	0.780	0.701	0.890	0.799	0.594	1.162	0.739	0.715	0.847	0.714	0.863	0.865	0.657
Dy/Yb	2.019	1.930	1.941	1.923	1.841	1.870	1.910	2.020	1.541	2.106	1.747	1.793	1.925	1.750	1.930	1.877	1.883
Plagioclase							43.1										33.8
K-feldspar							12.7										20.1
Quartz							9.0										24.7
Amphibole							5.6										6.4
Biotite							6.5										8.5
Pyroxene							9.6										3.6
Chlorite							10.5										1.3
Fe-Ti Oxides							1.1										1.3
Additional Phases							2.0										0.3
TOTAL							100.0										100.0

(*continued*)

TABLE 3. ABBREVIATED WHOLE-ROCK GEOCHEMISTRY RESULTS AND MODAL PHASE COMPOSITIONS (*continued*)

Sample identity						Maronia												
	RT14-010	RT14-015	RT14-017	RT14-022	RT14-024	MA15_015	MA15-004	MA15-006	MA15-007	MA15-008	MA15-010	MA15-011	MA15-012	MA15-014	MA15-016	MA15-017	MA15-020	RT14_006
SiO_2 (wt%)	67.340	53.600	48.270	58.900	56.140	51.160	55.270	50.410	51.100	52.110	52.910	54.710	53.320	55.570	53.000	55.720	53.430	52.930
TiO_2 (wt%)	0.400	0.840	1.130	0.710	0.630	0.880	0.850	1.070	0.920	0.870	0.980	0.900	0.960	0.850	1.000	0.820	0.910	0.730
Al_2O_3 (wt%)	15.370	18.150	20.640	15.690	13.630	15.890	16.260	16.040	15.160	15.240	16.690	16.550	16.890	16.080	16.740	14.910	16.270	19.840
$Fe_2O_3^T$ (wt%)	4.150	9.090	9.950	6.710	8.480	9.940	7.350	9.990	9.350	8.760	9.160	8.240	8.770	7.570	8.790	7.400	8.340	6.140
Mn_3O_4 (wt%)	0.100	0.180	0.170	0.160	0.140	0.180	0.140	0.200	0.170	0.170	0.170	0.170	0.170	0.140	0.170	0.150	0.160	0.120
MgO (wt%)	1.550	4.540	4.280	3.950	6.600	6.310	4.170	5.800	7.060	6.620	4.750	4.060	4.550	4.150	4.450	5.560	4.580	3.590
CaO (wt%)	2.860	7.980	10.740	3.820	6.900	9.580	7.040	9.680	10.190	9.660	8.280	7.250	7.890	6.570	7.760	7.870	7.400	8.810
Na_2O (wt%)	2.990	2.810	2.510	3.010	2.620	2.610	2.870	2.530	2.420	2.490	2.800	2.890	2.860	2.830	2.700	2.640	2.650	3.130
K_2O (wt%)	3.210	1.300	0.890	3.740	3.020	2.620	4.290	2.710	2.220	2.750	3.070	3.500	3.240	4.680	4.020	4.350	4.330	3.050
P_2O_5 (wt%)	0.090	0.120	0.130	0.150	0.190	0.610	0.500	0.640	0.590	0.570	0.470	0.420	0.460	0.560	0.520	0.500	0.600	0.430
LOI	1.550	1.270	0.940	2.220	1.320	0.170	0.290	0.130	0.350	0.080	0.570	0.520	0.420	-0.040	0.210	0.110	0.250	0.930
Total	99.610	99.880	99.650	99.060	99.670	99.950	99.030	99.200	99.530	99.320	99.850	99.210	99.530	98.960	99.360	100.030	98.920	99.700
Rb (ppm)	71.000	38.000	19.000	103.000	80.000	106.000	168.000	107.000	92.000	96.000	123.000	127.000	135.000	208.000	150.000	178.000	174.000	134.000
Sr (ppm)	257.000	380.000	533.000	396.000	291.000	689.000	606.000	717.000	685.000	677.000	702.000	617.000	693.000	604.000	665.000	536.000	694.000	924.000
Ba (ppm)	990.000	418.000	248.000	999.000	618.000	1029.000	1216.000	1208.000	746.000	960.000	994.000	813.000	1004.000	1293.000	1320.000	1178.000	1594.000	727.000
Eu/Eu*	0.798	0.814	0.797	0.721	0.645	0.781	0.778	0.763	0.880	0.838	0.789	0.735	0.811	0.724	0.819	0.744	0.778	1.080
Dy/Yb	1.552	1.930	2.173	1.623	1.743	2.175	2.166	2.228	2.233	2.137	2.145	1.970	1.909	2.000	2.109	2.332	2.181	2.145
Plagioclase	45.6	66.7	64.0	67.6	32.4													33.8
K-feldspar	13.2	0.0	0.0	0.0	19.7													37.9
Quartz	26.5	0.0	5.7	1.4	9.3													0.2
Amphibole	1.4	22.4	17.0	0.0	15.2													10.0
Biotite	0.7	9.0	0.3	0.0	0.3													7.6
Pyroxene	0.0	0.0	4.4	2.1	7.3													3.6
Chlorite	11.1	0.0	2.5	21.9	14.4													4.2
Fe-Ti Oxides	1.4	2.0	6.0	7.0	1.4													2.4
Additional Phases	0.0	0.0	0.0	0.0	0.0													0.4
TOTAL	100.0	100.0	100.0	100.0	100.0													100.0

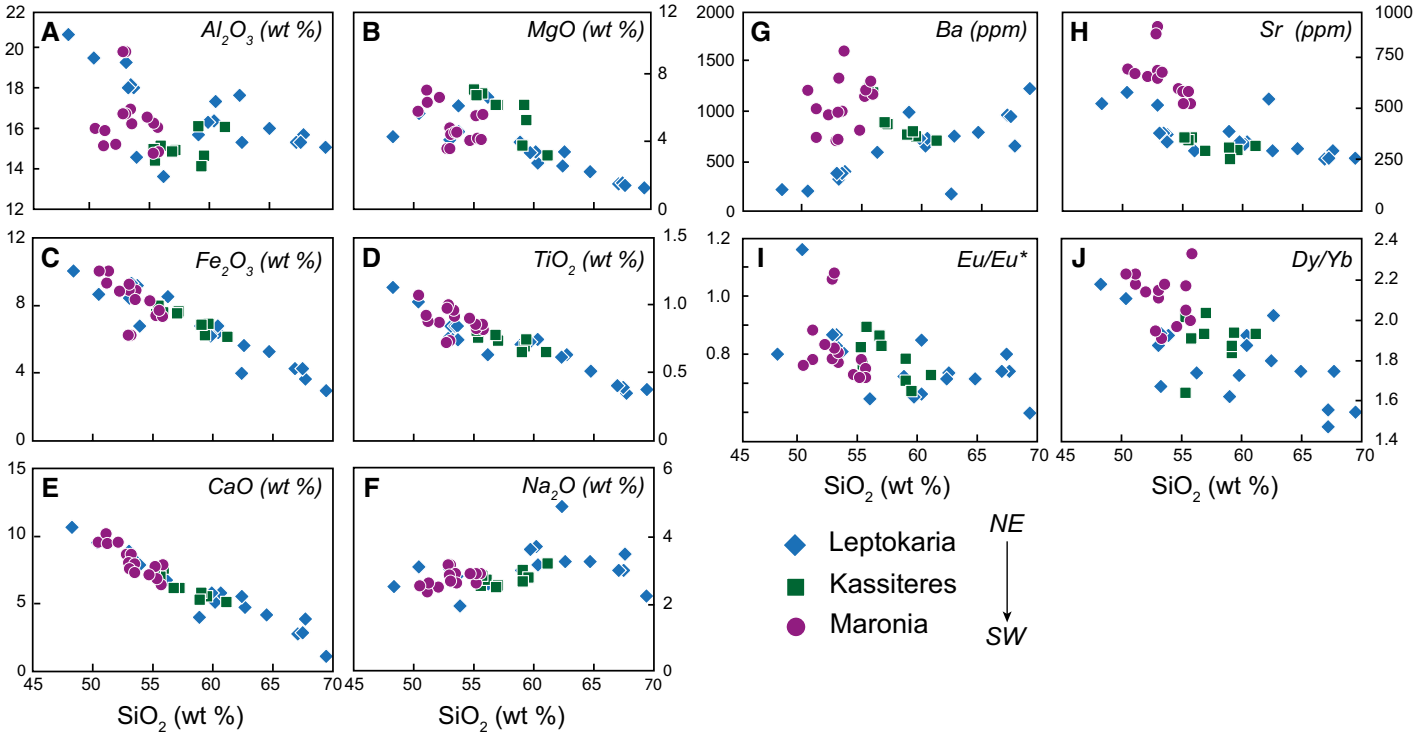

Figure 6. Element, oxide, or elemental ratio versus SiO_2 Harker plots; only data from this study is plotted for clarity of interpretation. (A–F) Major element versus SiO_2 plots show a liquid line of descent in each of the sample suites. (G–H) Ba/Sr versus SiO_2 plots show elevated concentrations of highly incompatible elements in the Maronia samples relative to Kassiteres and Leptokaria; in both magmatic suites Sr behaves as a compatible element. (I) Eu/Eu* vs. SiO_2 shows a trend of decreasing Eu/Eu*, an increasingly negative Eu anomaly, with fractionation. The Leptokaria cumulate samples (<53 wt% SiO_2) have a considerable, negative Eu anomaly (<0.9). (J) Dy/Yb vs SiO_2 shows negative correlation showing fractionation of a middle rare earth element–compatible phase, amphibole or pyroxene, during crystallization.

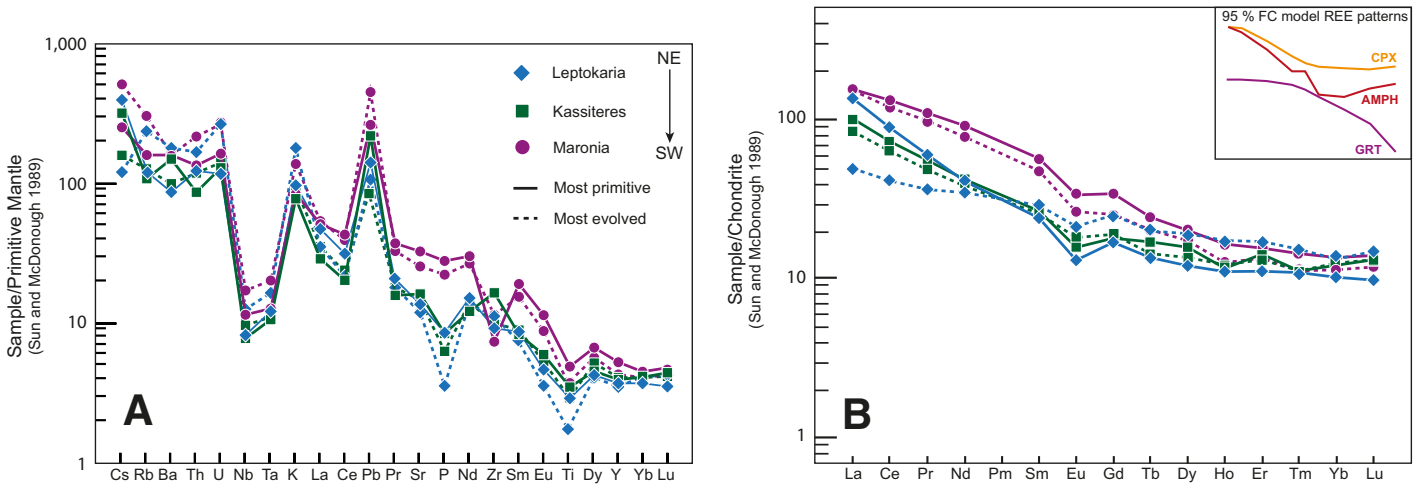

Figure 7. (A) Trace element spider plot; the irregular shape is typical of an enriched, metasomatic mantle signal. The Maronia Magmatic Corridor (MMC) shows elevated high field strength elements: Cs, Rb, Ba, Th, and U, and depleted large ion lithophile elements: Nb and Ta. Maronia shows elevated Sr, P, Nd, and Sm typical of a shoshonitic magma. (B) Rare earth element (REE) spider plot; the MMC shows a consistent negative Eu anomaly and moderately curved shape. Maronia is enriched in the light REEs (La to Sm) relative to Kassiteres and Leptokaria, which is again indicative of shoshonitic magmatism. The inset shows the modeled normalized REE shapes at 95% fractional crystallization for clinopyroxene (CPX), amphibole (AMPH), and garnet (GRT) for a source mineral composition of 70% olivine, 30% clinopyroxene or 70% olivine, 25% clinopyroxene, and 5% amphibole/garnet after Davidson et al. (2013).

TABLE 4. SUMMARY OF THE $^{206}PB/^{238}U$ INTERPRETED AGES FOR THE MARONIA MAGMATIC CORRIDOR

Sample name	Intrusive complex	$^{206}Pb/^{238}U$ date (Ma)	± (*x*)	± (*y*)	MSWD	n	Justification
RT14-010	Leptokaria-Kassiteres	32.932	0.034	0.052	2.00	6/6	Weighted mean (all)
RT14-009	Leptokaria-Kassiteres	32.235	0.026	0.047	2.20	6/7	Weighted mean (excluding high Pb_c zircon)
RT14-022	Leptokaria-Kassiteres	32.38	0.030	0.049	–	–	Youngest date
RT14-024	Leptokaria-Kassiteres	32.06	0.070	0.080	–	–	Youngest date
RT14-028	Leptokaria-Kassiteres	32.045	0.020	0.044	1.15	3/5	Youngest three dates (weighted mean)
MN16-008	Maronia	29.743	0.030	0.047	2.00	5/5	Weighted mean (all)
MN16-005	Maronia	29.762	0.017	0.040	0.84	4/4	Weighted mean (all)
RT14-003	Maronia	29.596	0.022	0.042	0.79	2/3	Youngest two dates (weighted mean)
MA15-010	Maronia	29.666	0.044	0.060	2.90	5/5	Weighted mean (all)

Note: *x* uncertainty—analytical only; *y* uncertainty—analytical + tracer calibration + ^{238}U decay constant. MSWD—mean square weighted deviation.

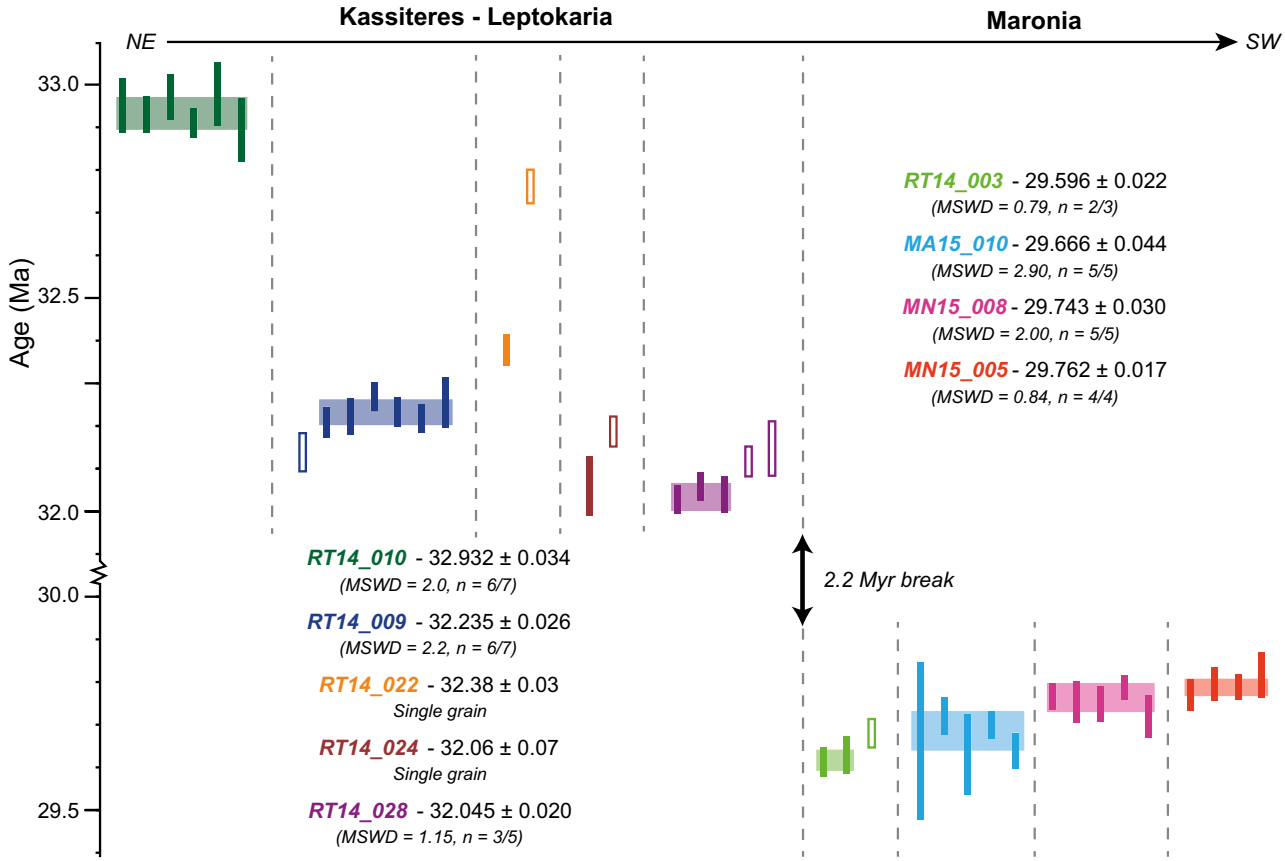

Figure 8. Geochronology dates for individual zircon crystals from Leptokaria–Kassiteres and Maronia. The solid bars represent analyses used to calculate the youngest single population from each sample and represent 2σ uncertainties; the open bars also represent 2σ uncertainties but are analyses that have been rejected from the youngest populations. There is a distinct temporal break between the age of crystallization of Kassiteres–Leptokaria between 33 and 32 Ma and Maronia between 30 and 29.5 Ma. MSWD—mean square weighted deviation.

Timescales of Magmatic Emplacement

Previous geochronological data from the MMC comprises nine Rb-Sr biotite–whole-rock pairs ranging from 34.9 ± 1.5–28.9 ± 1.5 Ma, which are interpreted to reflect an ~8 Myr window of magmatism along the MMC, younging from NE to SW (Del Moro et al., 1988). However, the Rb-Sr geochronometer is highly susceptible to disturbance by hydrothermal overprinting (Jenkin et al., 2001), and at least three of the MMC plutons are associated with significant hydrothermal activity (Melfos and Voudouris, 2017, and references therein). Our high-precision zircon CA-ID-TIMS U-Pb geochronological data show two tightly constrained magmatic windows: (i) 0.9 Myrs (from 32.045 ± 0.027–32.932 ± 0.039 Ma) for the Kassiteres–Leptokaria magmatic suite, and (ii) 0.2 Myrs (from 29.596 ± 0.027–29.762 ± 0.024) for the Maronia magmatic suite (Table 4; Fig. 8). These two discrete time periods are consistent with the distinct geochemical signature of Maronia compared to Kassiteres–Leptokaria.

Within the Kassiteres–Leptokaria magmatic suite, our data do not duplicate the younging of magmatic activity from NE to SW concluded by Del Moro et al. (1988). While the youngest and oldest samples, RT14_028 (32.045 ± 0.027 Ma) and RT14_010 (32.932 ± 0.039 Ma), respectively, do follow this SW-trend, the remaining three samples show ongoing crystallization in the intervening time period, consistent with pulsed magma accumulation across the pluton. This agrees with our earlier interpretation that there is potential for the Leptokaria outcrops to be connected at depth by a large, mostly unexposed magmatic system. The inter-sample age range (0.887 ± 0.039 Myrs at Leptokaria and 0.166 ± 0.028 Myrs at Maronia) reflects the time scale of pluton cooling. As the larger intrusive body, the duration of cooling of the Kassiteres–Leptokaria complex is nearly an order of magnitude greater than the Maronia pluton.

We emphasize that the high-precision U-Pb zircon geochronology presented in this paper shows a clear temporal break in exposed, intrusive magmatism in the MMC, reflecting two discrete magmatic periods. The first magmatic period produced the Kassiteres–Leptokaria magmatic suite and was followed, after an apparent 2.2 Myr break in recorded magmatism, by the Maronia plutonic complex.

Petrogenesis of the Kassiteres–Leptokaria Magmatic Suite

Equigranular, plutonic samples from the Kassiteres–Leptokaria magmatic suite record the first stage of post-collisional magmatism hosted in the southern Kechros dome. The high-K calc alkaline magmatic suite has trace element geochemistry that is consistent with a sub-continental lithospheric mantle source (Del Moro et al., 1988; Pe-Piper and Piper, 2001). The presence of hornblende phenocrysts in textural equilibrium with surrounding mineral phases (Fig. 3E) indicates crystallization of the magmatic suite at a depth of >~3 km (Lledo and Jenkins, 2007; Mutch et al., 2016). The intrusions show granophyric interstitial textures reflecting fast cooling of the last vestiges of melt during rapid final crystallization.

The major and minor element geochemistry of the Kassiteres–Leptokaria suite, most notably the steadily depleting Al_2O_3 with fractionation, the consistently negative Eu anomaly, and the compatible behavior of Sr, suggest plagioclase was an important phase during magmatic differentiation. The presence of abundant plagioclase in the Leptokaria samples with a cumulate-like texture further supports the early appearance of plagioclase on the liquidus (Table 3). This is atypical of arc-type magmatism where partial mantle melts with elevated water contents suppress plagioclase saturation (Gaetani et al., 1993). Decreasing Dy/Yb with fractionation (Fig. 6J) suggest clinopyroxene and/or amphibole are the predominant ferromagnesian phases controlling fractionation (Davidson et al., 2013). Amphibole is the most abundant phase in the cumulate-like samples (Table 3); however, relict subhedral clinopyroxene in the core of many of the amphibole phenocrysts (Fig. 3B) suggests clinopyroxene was a precursor to amphibole during fractionation. This can account for the more primitive REE pattern (Fig. 7B; Smith, 2014).

Experimental studies on the effect of intensive parameters: temperature (T), pressure (P), H_2O content, and oxygen fugacity (fO_2), on phase equilibria are commonly used to investigate the physiochemical conditions of magma differentiation, crystallization, and storage (e.g., Scaillet et al., 2016). Naney (1983) produced phase assemblage diagrams, at both 200 MPa (~6 km) and 800 MPa (~24 km), of fO_2 controlled granodiorite compositions as a function of T and H_2O content. The synthetic starting composition used by Naney (1983), "R5 + 10MI," and the natural analogue hornblende, biotite, granodiorite R5 (Nockolds, 1954), are similar in composition to the Leptokaria tonalities that make up the more evolved end member of Kassiteres–Leptokaria magmatism (GSA Data Repository Table DR1). Using the major fractionating assemblage of plagioclase + pyroxene + amphibole and the phase diagrams of Naney (1983), the T and H_2O field of lower crustal fractionation (at P = 800 MPa, 24 km) can be constrained to 880 < T < 980 °C and 3 < H_2O content < 4.75 wt% (Fig. 9). The drier nature of the magmas suggests that the fertile mantle source has been tapped by multiple different melting events during which H_2O has been mobilized, prior to the generation and emplacement of the Kassiteres–Leptokaria magmas between 32.9 and 32.0 Ma. We suggest that the elevated temperature necessary to melt a drier mantle wedge (>880 °C, Fig. 9) was provided by the accumulation of heat during prolonged (more than ~10 Myr) asthenospheric upwelling and mantle melting in the northern Aegean, which began in the mid-Eocene (e.g., Rohrmeier et al., 2013).

Petrogenesis of the Maronia Pluton

Maronia shows a different petrogenetic evolution to Kassiteres–Leptokaria, coincident with a 2.2 Myr temporal, and a 30 km spatial, break

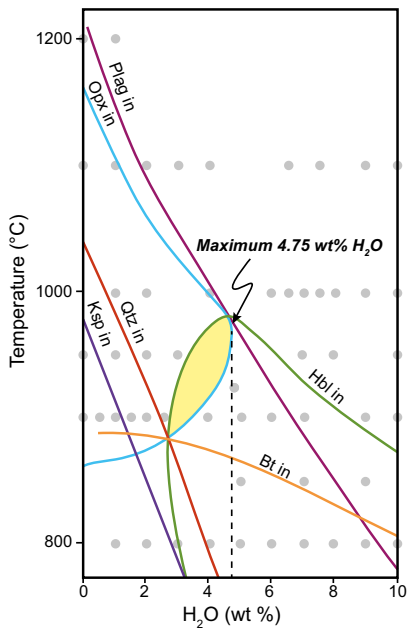

Figure 9. Phase relations of synthetic granodiorite (R5 + 10M1) at 800 MPa, expanded from figure 4A *in* Naney (1983). The colored lines indicate the stability field of each phase. Phase abbreviations: Plag—plagioclase; Opx—orthopyroxene; Hbl—hornblende; Qtz—quartz; Ksp—alkali feldspar; Bt—biotite. Each gray circle indicates an experiment performed by Naney (1983). The synthetic granodiorite has a similar composition to samples RT14_010 and LB15_004, and the hornblende-biotite granodiorite sample it is based on is similar in composition to LC15_003. Our whole-rock geochemistry trace elements and rare earth element patterns indicate plagioclase and pyroxene are the primary minerals controlling deep crustal fractionation of the Kassiteres-Leptokaria suite. The yellow shaded area indicates the Plag + Opx + Hbl stability field for this composition and indicates a maximum water content of 4.75wt% H_2O.

in recorded magmatism. The Maronia monzonite has a shoshonitic affinity with significant enrichment in incompatible and volatile elements (e.g., P_2O_5, Pb, Sr, Rb; Figs. 5B, 6G, 6H). Geochemical and isotopic evidence advocate a heterogeneous, highly metasomatized source mantle as the foundation for the generation of ultra-potassic shoshonitic to lamproitic magmas (e.g., Foley et al., 1987; Beccaluva et al., 2013; Condamine and Médard, 2014; Müller and Groves, 2016). Sr isotopic data from the MMC reported by Del Moro et al. (1988; Table 4), show consistently enriched radiogenic ^{87}Sr across the Kassiteres–Leptokaria ($^{87}Sr/^{86}Sr$ = 0.7057–0.7080) and Maronia ($^{87}Sr/^{86}Sr$ = 0.7061–0.7076) magmatic suites. This is unlike the Sr isotopic data reported from the Eocene–Oligocene Biga orogenic volcanic rocks, NW Turkey, where the magmatic suite becomes increasingly radiogenic and potassic with time, which is interpreted to reflect an increasing crustal contribution (Ersoy et al., 2017). Consequently, we suggest that the MMC source mantle was enriched by a radiogenic source, likely crustal-derived metasomatic fluids, prior to the start of high-K calc-alkaline magmatism at Kassiteres–Leptokaria. Therefore, processes involved in magma generation and fractionation were responsible for the evolution of a shoshonitic trend at Maronia. Further to this, experimental data for the contamination and mixing of mantle and sedimentary melts in the production of a K-rich starting melt generate evolved, peraluminous shoshonitic magmas (Wang et al., 2017) while the Maronia magmatic suite has a highly restricted SiO_2 (51–56 wt% SiO_2) range and is metaluminous.

Melting of a phlogopite-rich veinlet in the highly metasomatized source mantle could be a potential source of an anomalously K-rich melt from which to fractionate a shoshonitic trend (e.g., Condamine and Médard, 2014). Such melts would inherit a diagnostic trace element pattern due to the compatible nature of LILEs (e.g., Rb and Ba) and incompatible nature of HFSEs (e.g., Zr and Y) in phlogopite (LaTourette et al., 1995). However, the Maronia samples show a relative enrichment in Rb and Ba over the Kassiteres–Leptokaria suite and similar values of Zr and Y (Fig. 7A). Direct mantle melts would be expected to have a Mg# = 80 – 85 (Mg# = Mg/(Mg + Fe^{2+}) * 100; molar), which will decrease with fractionation (Herzberg et al., 2014). The Mg# of the Maronia shoshonites ranges from 49.4 < Mg # < 60.2 indicating that significant fractionation from direct lherzolitic or harzburgitic mantle would be required to produce the potassic fractionation trend observed at Maronia. Therefore we favor the model of pyroxene + An-rich plagioclase + magnetite fractionation in the absence of major olivine, in an H_2O-poor magma, as a mechanism to produce a shoshonitic LLD (Meen, 1987; Freise et al., 2009; Lanzo et al., 2016; Beermann et al., 2017).

We have modeled fractional crystallization by subtracting varying proportions of the proposed orthopyroxene + clinopyroxene + An-rich plagioclase + magnetite fractionating assemblage (Meen, 1987; Beermann et al., 2017), from the most primitive known sample from Maronia (MP 81; Mavroudchiev et al., 1993). We do not include olivine in our fractionating assemblage as we consider it to be a minor phase in the generation of a LLD (Meen, 1987) and we assume K_2O to be incompatible during fractionation (Freise et al., 2009). The observed fractionation trend from the parent magma can be closely matched by a modeled fractionation assemblage of 15% orthopyroxene (En 0.8), 25% clinopyroxene (Di 0.8), 52% plagioclase (An 75) and 8% magnetite (Mag 0.7; Figure 10A; Table 5). The close agreement between the modeled and observed LLDs suggests that fractionation of pyroxene + plagioclase (+ minor magnetite), which have higher silica content than olivine (OL ~30 wt% SiO_2; OPX ~50 wt% SiO_2; CPX ~45 wt% SiO_2; PLAG ~50 wt% SiO_2), can sufficiently enrich the residual magma in incompatible elements with small changes in melt SiO_2, to produce a shoshonitic LLD (Meen, 1987; Beermann et al., 2017). Using the predicted fractionating phase assemblage and estimated bulk

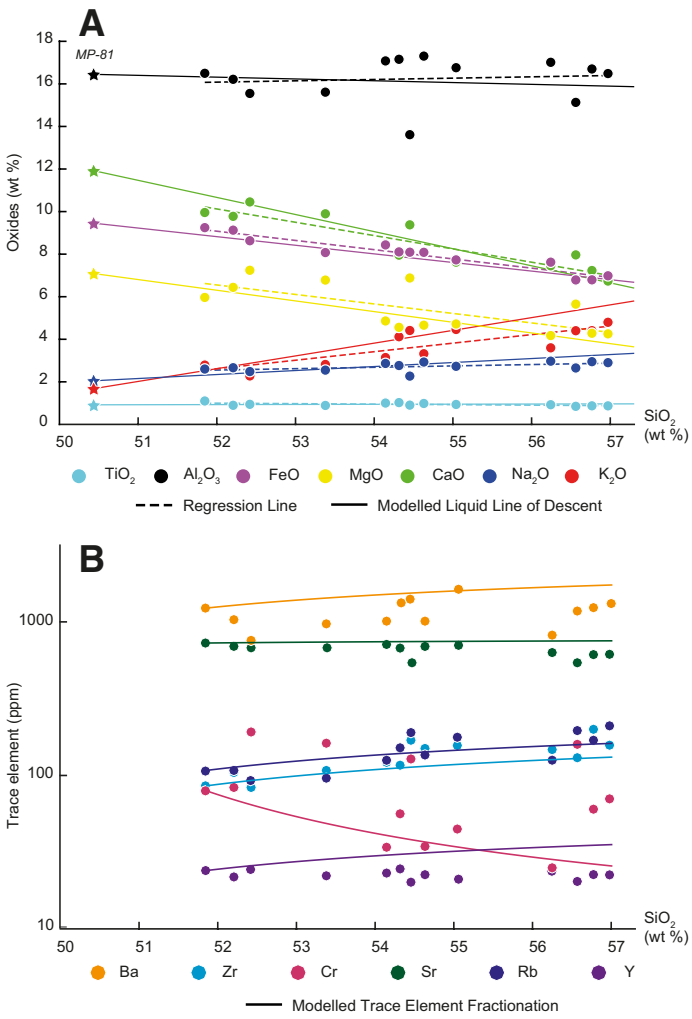

Figure 10. Modeled major (A) and trace element (B) distribution during clinopyroxene + orthopyroxene + plagioclase + magnetite fractionation in the absence of olivine (after Meen, 1987). The distribution of Maronia samples can be closely reproduced by the model; see Table 5 for details of fractionating phase compositions and proportions and Table 6 for the partition coefficients for the trace element modeling (McKenzie and O'Nions, 1991; Hart and Dunn, 1993; Bindeman et al., 1998; Green et al., 2000; Adam and Green, 2006).

partition coefficients (Table 6), the observed trace element fractionation trends can be reproduced and are shown in Figure 10B for Ba, Cr, Rb, Sr, Zr, and Y.

A pyroxene + plagioclase + magnetite fractionating assemblage can be produced by an H_2O-poor (<2–3 wt% H_2O) magma at high-*T* (950–1050 °C) and a range of pressures (200–1,000 MPa; Baker and Eggler, 1987; Meen, 1987; Beermann et al., 2017). This suggests that fractionation of the same parental mantle source region as Kassiteres–Leptokaria could produce a shoshonitic trend with a similar trace element signature as the Maronia pluton by losing H_2O. In a post-collisional setting, H_2O is a finite resource. Thus, if moderately wet magmas (<4.75 wt% H_2O) were produced in the generation of the Kassiteres–Leptokaria magmatic suite driving the H_2O content of the parental source region down, the later Maronia magmas could be generated from an H_2O-poor (<~2 wt%) source region in which pyroxene + plagioclase are stable instead of olivine. The generation of shoshonitic magmas at Maronia requires a change in mantle

TABLE 5. SUMMARY OF THE FRACTIONATION MODEL

	SiO_2 (wt %)	TiO_2 (wt %)	Al_2O_3 (wt %)	FeO (wt %)	MgO (wt %)	CaO (wt %)	Na_2O (wt %)	K_2O (wt %)	Model proportions
MP 81 (starting composition)	49.28	0.90	16.08	9.25	6.94	11.67	2.00	1.63	–
Clinopyroxene	54.08	–	–	5.79	14.89	25.24	–	–	15%
Orthopyroxene	56.99	–	–	10.89	32.12	–	–	–	25%
Plagioclase	49.58	–	32.35	–	–	15.113	2.96	–	52%
Magnetite	–	10.72	–	89.28	–	–	–	–	8%

Note: MP-81 was chosen as the starting composition as it had the most primitive mantle signature (a combination of low SiO_2, high Mg# and high Ni, Cr concentrations). The predicted liquid lines of descent can be found in Figure 10 plotted alongside the whole-rock analyses.

TABLE 6. THE TRACE ELEMENT MINERAL:MELT PARTITION COEFFICIENTS USED FOR FRACTIONATION MODELING

	Sr (ppm)	Ba (ppm)	Cr (ppm)	Rb (ppm)	Zr (ppm)	Y (ppm)
Clinopyroxene	0.128 (a)	0.0007 (a)	3.8 (a)	0.011 (b)	0.123 (a)	0.47 (a)
Orthopyroxene	0.0012 (c)	0.004 (d)	7.8 (d)	0.004 (d)	0.032 (c)	0.095 (c)
Plagioclase	2 (e)	0.5 (e)	0.08 (e)	0.2 (e)	0.006 (e)	0.01 (e)

Note: (a)—Hart and Dunn (1993); (b)—McKenzie and O'Nions (1991); (c)—Green et al. (2000); (d)—Adam and Green (2006); (e)—Bindeman et al. (1998).

melting conditions between the intrusion of the Kassiteres–Leptokaria magmatic complex and intrusion of the Maronia pluton. We suggest that the temporal break (2.2 Myrs) in recorded magmatism in the MMC is the result of H_2O loss in the source mantle driving up the solidus temperature such that, between intrusion of Kassiteres–Leptokaria and Maronia, the source mantle was at sub-solidus conditions. We propose that prolonged heat conduction from the upwelling thermal anomaly beneath the Kechros dome in the intervening 2.2 Myrs is a potential source for the additional heat input required. Resultant melting of the H_2O-poor source mantle stabilized a pyroxene + plagioclase–dominated fractionating assemblage and generated a shoshonitic LLD at Maronia. A similar mechanism of restricted H_2O flux into a metasomatized mantle source is suggested for the generation of the shoshonitic volcanics in the Aeolian arc, Italy (e.g., Peccerillo et al., 2013; Beermann et al., 2017).

Summary of Magmatism and Extension in the Northern RCC

Post-collisional magmatism in the northern RCC began in the mid-Eocene, contemporaneous with a period of trans-crustal extension and core complex exhumation, and continued into the Oligocene (Table 2; e.g., Marchev et al., 2005; Rohrmeier et al., 2013). This phase of post-collisional extension is attributed to the collapse of thickened orogenic lithosphere induced by slab rollback of the N-ward subducting African plate (e.g., Jolivet and Brun, 2010; Ring et al., 2010; Burg, 2011; Kydonakis et al., 2015). Eocene–Oligocene magmatism from across the northern RCC has a strong enriched metasomatic mantle signature, the result of asthenospheric mantle upwelling beneath thinned lithosphere remobilizing and re-melting the subcontinental lithospheric mantle (e.g., Pe-Piper et al., 2009).

In the Kechros dome, Eocene crustal extension was accommodated by tectonic unroofing of the lower-crustal gneisses along the Kechros detachment fault, a trans-crustal structure that would be later exploited by post-collisional magmatism (Marchev et al., 2010; Márton et al., 2010). An Oligocene, high-K calc-alkaline magmatic event at 32.9–32.0 Ma in the southern Kechros dome resulted in the intrusion of the Kassiteres–Leptokaria magmatic suite, a high-K calc-alkaline series of intrusions with a strong subduction-related sub-continental lithospheric mantle signature. Following a 2.2 Myr break in magmatism, the intrusion of the shoshonitic Maronia pluton marks the last magmatic activity in the Kechros dome prior to tectonic change. The potassic intrusion, enriched in incompatible and volatile elements, marks an anomalously hot, short period of magmatism in the Kechros dome. Melting of a now H_2O-poor (<~2 wt% H_2O) mantle source fractionated plagioclase + pyroxene to produce the Maronia intrusion and marked the culmination of asthenospheric heating of a mature, Cretaceous metasomatized lithospheric mantle. We suggest that the termination of magmatism in the Kechros dome following the intrusion of the Maronia pluton at 29.6 Ma reflects the southward migration of the asthenospheric upwelling, switching off the heat source for mantle melting beneath the Kechros dome. We hypothesize that the asthenospheric upwelling migration is co-incident with initiation of SW-rotation of the southern RCC as described by van Hinsbergen et al. (2008) and others. The continuation of post-collisional magmatism in the southern RCC, such as the Miocene shoshonitic magmatism in Samothraki (e.g., Christofides et al., 2000) and Skouries (e.g., Siron et al., 2016) reflects the persistence of asthenospheric upwelling beneath the southern RCC and melting of the mature, H_2O-poor (<~2 wt% H_2O) mantle wedge.

CONCLUSIONS

The MMC intrusions provide chronological markers and geochemical tracers that record the petrogenetic evolution of magmatism in the Kechros dome, northern RCC. Late Cretaceous to Oligocene extension of the northern Aegean resulted in asthenospheric mantle upwelling beneath the northern RCC, which provided a heat source for re-melting of the Cretaceous metasomatized mantle wedge. High-precision geochronology coupled with a full suite of whole-rock geochemical analyses, detailed field and petrographic observations, and petrological modeling demonstrate that:

1. The MMC does not represent a continuous magmatic period between 35 and 28 Ma (Del Moro et al. 1988) but two, temporally and geochemically distinct, magmatic complexes, the Kassiteres–Leptokaria magmatic suite and the Maronia plutonic complex. Intrusion of Kassiteres–Leptokaria was between 32.05 ± 0.02 and 32.93 ± 0.02 Ma, while magmatism at Maronia lasted from 29.60 ± 0.02–29.76 ± 0.02 Ma. In addition, it is recommended that the MMC zircon U-Pb data presented here are used in preference to Del Moro et al. (1988) to constrain the timing of magmatic activity in the MMC;

2. Extended hydrous (3 < H_2O content < 4.75 wt%) partial mantle melting beneath the northern RCC allowed for the intrusion of batches

of lithospheric mantle-source magma over an ~900,000 year time scale at Kassiteres–Leptokaria;

3. The shoshonitic affinity of the Maronia samples reflects incompatible element enrichment produced by plagioclase + pyroxene–controlled mantle fractionation from a source mantle highly depleted in H_2O (<~2 wt% H_2O); and therefore,

4. The temperature of mantle melting beneath the Kechros dome increased between intrusion of the Kassiteres–Leptokaria magmatic suite (at 32.9–32.0 Ma) and the Maronia pluton (29.8–29.6 Ma). Consequently, we suggest that the apparent 2.2 Myr break in recorded magmatism could be the result of a sub-solidus lithospheric mantle, and that heat accumulation in the intervening time period provided the heat required for the renewal of mantle melting.

ACKNOWLEDGMENTS

This work was funded by a NERC GW4+ UK Doctoral Training Partnership Studentship (Grant NE/L002434/1) and in part by the BGS University Funding Initiative (S276), which are gratefully acknowledged. Supporting data are provided within this paper and the GSA Data Repository (Item 2018177). Ben Buse and Stuart Kearns are thanked for their help with SEM analysis, and Dr. C. Gowing at the Inorganic Geochemical Facility at the British Geological Survey for the whole-rock geochemistry analyses. We would like to thank Katerina Gkika, Ery Hughes, and Simon Dahlström for assistance in the field, and the petrological modeling benefited greatly from discussions with Robert Loucks. D.J. Condon and J. Naden publish with the permission of the Executive Director, British Geological Survey (NERC). We thank Alexandre Kounov and two anonymous reviewers for their expert reviews, which have greatly improved the manuscript.

REFERENCES CITED

Adam, J., and Green, T., 2006, Trace element partitioning between mica-and amphibole-bearing garnet lherzolite and hydrous basanitic melt: 1. Experimental results and the investigation of controls on partitioning behaviour: Contributions to Mineralogy and Petrology, v. 152, p. 1–17, https://doi.org/10.1007/s00410-006-0085-4.

Aldanmaz, E., Pearce, J.A., Thirlwall, M.F., and Mitchell, J.G., 2000, Petrogenetic evolution of late Cenozoic, post-collision volcanism in western Anatolia, Turkey: Journal of Volcanology and Geothermal Research, v. 102, p. 67–95, https://doi.org/10.1016/S0377-0273(00)00182-7.

Baker, D.R., and Eggler, D.H., 1987, Compositions of anhydrous and hydrous melts coexisting with plagioclase, augite, and olivine or low-Ca pyroxene from 1 atm to 8 kbar: Application to the Aleutian volcanic center of Atka: The American Mineralogist, v. 72, p. 12–28.

Bauer, C., Rubatto, D., Krenn, K., Proyer, A., and Hoinkes, G., 2007, A zircon study from the Rhodope metamorphic complex, N-Greece: Time record of a multistage evolution: Lithos, v. 99, p. 207–228, https://doi.org/10.1016/j.lithos.2007.05.003.

Beccaluva, L., Bianchini, G., Mameli, P., and Natali, C., 2013, Miocene shoshonite volcanism in Sardinia: Implications for magma sources and geodynamic evolution of the central-western Mediterranean: Lithos, v. 180–181, p. 128–137, https://doi.org/10.1016/j.lithos.2013.08.006.

Beermann, O., Holtz, F., and Duesterhoeft, E., 2017, Magma storage conditions and differentiation of the mafic Lower Pollara volcanics, Salina Island, Aeolian Islands, Italy: Implications for the formation conditions of shoshonites and potassic rocks: Contributions to Mineralogy and Petrology, v. 172, p. 37, https://doi.org/10.1007/s00410-017-1363-z.

Bindeman, I.N., Davis, A.M., and Drake, M.J., 1998, Ion microprobe study of plagioclase-basalt partition experiments at natural concentration levels of trace elements: Geochimica et Cosmochimica Acta, v. 62, p. 1175–1193, https://doi.org/10.1016/S0016-7037(98)00047-7.

Bonev, N., and Stampfli, G., 2008, Petrology, geochemistry and geodynamic implications of Jurassic island arc magmatism as revealed by mafic volcanic rocks in the Mesozoic low-grade sequence, eastern Rhodope, Bulgaria: Lithos, v. 100, p. 210–233, https://doi.org/10.1016/j.lithos.2007.06.019.

Bonev, N., and Stampfli, G., 2011, Alpine tectonic evolution of a Jurassic subduction-accretionary complex: Deformation, kinematics and $^{40}Ar/^{39}Ar$ age constraints on the Mesozoic low-grade schists of the Circum-Rhodope Belt in the eastern Rhodope-Thrace region, Bulgaria-Greece: Journal of Geodynamics, v. 52, p. 143–167, https://doi.org/10.1016/j.jog.2010.12.006.

Bonev, N., Ovtcharova-Schaltegger, M., Moritz, R., Marchev, P., and Ulianov, A., 2013, Peri-Gondwanan Ordovician crustal fragments in the high-grade basement of the Eastern Rhodope Massif, Bulgaria: Evidence from U-Pb LA-ICP-MS zircon geochronology and geochemistry: Geodinamica Acta, v. 26, p. 207–229, https://doi.org/10.1080/09853111.2013.858942.

Bonev, N., Marchev, P., Moritz, R., and Collings, D., 2015, Jurassic subduction zone tectonics of the Rhodope Massif in the Thrace region (NE Greece) as revealed by new U-Pb and $^{40}Ar/^{39}Ar$ geochronology of the Evros ophiolite and high-grade basement rocks: Gondwana Research, v. 27, p. 760–775, https://doi.org/10.1016/j.gr.2014.08.008.

Bornovas, J., and Rondogianni-Tsiabaou, T., 1983, Geological Map of Greece (1:50,000), 2nd Edition: Institute of Geology and Mining Exploration, Athens, Greece.

Boyanov, I., Ruseva, M., and Dimitrova, E., 1982, First find of Upper Cretaceous foraminifers in East Rhodopes: Geologica Balcanica, v. 12, p. 20.

Brun, J., Faccenna, C., Gueydan, F., Sokoutis, D., Philippon, M., Kydonakis, K., and Gorini, C., 2016, The two-stage Aegean extension, from localized to distributed, a result of slab rollback acceleration: Canadian Journal of Earth Sciences, v. 53, no. 11, p. 1142–1157, https://doi.org/10.1139/cjes-2015-0203.

Burchfiel, B.C., Nakov, R., and Tzankov, T., 2003, Evidence from the Mesta half-graben, SW Bulgaria, for the Late Eocene beginning of Aegean extension in the Central Balkan Peninsula: Tectonophysics, v. 375, p. 61–76, https://doi.org/10.1016/j.tecto.2003.09.001.

Burchfiel, B.C., Nakov, R., Dumurdzanov, N., Papanikolaou, D., Tzankov, T., Serafimovski, T., King, R.W., Kotzev, V., Todosov, A., and Nurce, B., 2008, Evolution and dynamics of the Cenozoic tectonics of the South Balkan extensional system: Geosphere, v. 4, p. 919–938, https://doi.org/10.1130/GES00169.1.

Burg, J., 2011, Rhodope: From Mesozoic convergence to Cenozoic extension. Review of petrostructural data in the geochronological frame: Journal of the Virtual Explorer, v. 39, p. 1–44, https://doi.org/10.3809/jvirtex.2011.00270.

Camp, V.E., Pierce, K.L., and Morgan, L.A., 2015, Yellowstone plume trigger for Basin and Range extension, and coeval emplacement of the Nevada–Columbia Basin magmatic belt: Geosphere, v. 11, p. 203–225, https://doi.org/10.1130/GES01051.1.

Christofides, G., Eleftheriadis, G., Esson, J., Soldatos, T., Koroneos, A., and Brocker, M., 2000, The evolution of the Samothraki granitic pluton (N. Aegean sea, Greece): Geochronology, chemical and isotopic constraints for AFC modelling, *in* Proceedings of the Third International Conference on the Geology of the Eastern Mediterranean, p. 193–209.

Condamine, P., and Médard, E., 2014, Experimental melting of phlogopite-bearing mantle at 1 GPa: Implications for potassic magmatism: Earth and Planetary Science Letters, v. 397, p. 80–92, https://doi.org/10.1016/j.epsl.2014.04.027.

Coney, P.J., 1987, The regional tectonic setting and possible causes of Cenozoic extension in the North American Cordillera, *in* Coward, M.P., Dewey, J.F., and Hancock, P.L, eds., Continental Extensional Tectonics: Geological Society, London, Special Publication 28, p. 177–186, https://doi.org/10.1144/GSL.SP.1987.028.01.13.

Cornelius, N.K., 2008, UHP metamorphic rocks of the Eastern Rhodope Massif, NE Greece: New constraints from petrology, geochemistry and zircon ages [PhD thesis]: Germany, Johannes Gutenberg-Universität Mainz, 1–173 p.

Crowley, J.L., Schoene, B., and Bowring, S.A., 2007, U-Pb dating of zircon in the Bishop Tuff at the millennial scale: Geology, v. 35, p. 1123–1126, https://doi.org/10.1130/G24017A.1.

Davidson, J., Turner, S., and Plank, T., 2013, Dy/Dy*: Variations arising from mantle sources and petrogenetic processes: Journal of Petrology, v. 54, p. 525–537, https://doi.org/10.1093/petrology/egs076.

Del Moro, A., Innocenti, F., Kyriakopoulos, C., Manetti, P., and Papadopoulos, P., 1988, Tertiary granitoids from Thrace (Northern Greece): Sr isotopic and petrochemical data: Neues Jahrbuch für Mineralogie Abhandlungen, v. 159, p. 113–115.

Del Moro, A., Kyriakopoulos, K., Pezzino, A., Atzori, P., and Lo Giudice, A., 1990, The metamorphic complex associated to the Kavala plutonites: An Rb-Sr geochronological, petrological and structural study: Geologica Rhodopica, v. 2, p. 143–152.

De Wet, A.P., Miller, J.A., Bickle, M.J., and Chapman, H.J., 1989, Geology and geochronology of the Arnea, Sithonia and Ouranopolis intrusions, Chalkidiki peninsula, northern Greece: Tectonophysics, v. 161, p. 65–79, https://doi.org/10.1016/0040-1951(89)90303-X.

Dewey, J.F., 1988, Extensional collapse of orogens: Tectonics, v. 7, p. 1123–1139, https://doi.org/10.1029/TC007i006p01123.

Dewey, J.F., Ryan, P.D., and Andersen, T.B., 1993, Orogenic uplift and collapse, crustal thickness, fabrics and metamorphic phase changes: The role of eclogites, *in* Prichard, H.M., Alabaster, T., Harris, N.B.W., and Neary, C.R., eds., Magmatic Processes and Plate Tectonics: Geological Society, London, Special Publications 76, p. 325–343, https://doi.org/10.1144/GSL.SP.1993.076.01.16.

Dinter, D.A., Macfarlane, A., Hames, W., Isachsen, C., Bowring, S., Royden, L., and Park, M., 1995, U-Pb and $^{40}Ar/^{39}Ar$ geochronology of the Symvolon granodiorite: Implications for the thermal and structural evolution of the Rhodope metamorphic core complex, northeastern Greece: Tectonics, v. 14, p. 886–908, https://doi.org/10.1029/95TC00926.

Dürr, S., Altherr, R., Keller, J., Okrusch, M., and Seidel, E., 1978, The median Aegean crystalline belt: Stratigraphy, structure, metamorphism, magmatism: Alps, Apennines: Hellenides, v. 38, p. 455–476.

Eleftheriadis, G., Frank, W., and Petrakakis, K., 2001, $^{40}Ar/^{39}Ar$ dating and cooling history of the Pangeon granitoids, Rhodope Massif (eastern Macedonia, Greece): Bulletin of the Geological Society of Greece, v. 34, p. 911–916.

Elliott, T., Plank, T., Zindler, A., White, W., and Bourdon, B., 1997, Element transport from slab to volcanic front at the Mariana arc: Journal of Geophysical Research, Solid Earth, v. 102, p. 14991–15019, https://doi.org/10.1029/97JB00788.

Ersoy, E.Y., Palmer, M.R., Genç, Ş. Can, Prelević, D., Akal, C., and Uysal, I., 2017, Chemo-probe into the mantle origin of the NW Anatolia Eocene to Miocene volcanic rocks: Implications for the role of, crustal accretion, subduction, slab roll-back and slab break-off processes in genesis of post-collisional magmatism: Lithos, v. 288, p. 55–71, https://doi.org/10.1016/j.lithos.2017.07.006.

Foley, S., Venturelli, G., Green, D.H., and Toscani, L., 1987, The ultrapotassic rocks: Characteristics, classification, and constraints for petrogenetic models: Earth-Science Reviews, v. 24, p. 81–134, https://doi.org/10.1016/0012-8252(87)90001-8.

Frei, R., 1996, The extent of inter-mineral isotope equilibrium: A systematic bulk U-Pb and Pb step leaching (PbSL) isotope study of individual minerals from the Tertiary granite of Jerissos (northern Greece): European Journal of Mineralogy, v. 8, no. 5, p. 1175–1190, https://doi.org/10.1127/ejm/8/5/1175.

Freise, M., Holtz, F., Nowak, M., Scoates, J.S., and Strauss, H., 2009, Differentiation and crystallization conditions of basalts from the Kerguelen large igneous province: An experimental study: Contributions to Mineralogy and Petrology, v. 158, p. 505, https://doi.org/10.1007/s00410-009-0394-5.

Gaetani, G.A., Grove, T.L., and Bryan, W.B., 1993, The Influence of water on the petrogenesis of subduction-related igneous rocks: Nature, v. 365, p. 332–334, https://doi.org/10.1038/365332a0.

Georgiev, S., Marchev, P., Peytcheva, I., von Quadt, A., and Vaselli, O., 2013, Miocene extensional magmatic activity along Strymon valley and Doyran region, Bulgaria, Greece and the former Yugoslav Republic of Macedonia: Acta Vulcanologica, v. 25, p. 153–168.

Gilg, H.A., and Frei, R., 1994, Chronology of magmatism and mineralization in the Kassandra mining area, Greece: The potentials and limitations of dating hydrothermal illites: Geochimica et Cosmochimica Acta, v. 58, p. 2107–2122, https://doi.org/10.1016/0016-7037(94)90289-5.

Gill, J.B., 1981, Orogenic Andesites and Plate Tectonics: Berlin Heidelberg, Springer-Verlag, 392 p., https://doi.org/10.1007/978-3-642-68012-0.

Green, T.H., Blundy, J.D., Adam, J., and Yaxley, G.M., 2000, SIMS determination of trace element partition coefficients between garnet, clinopyroxene and hydrous basaltic liquids at 2–7.5 GPa and 1080–1200 °C: Lithos, v. 53, p. 165–187, https://doi.org/10.1016/S0024-4937(00)00023-2.

Hart, S.R., and Dunn, T., 1993, Experimental cpx/melt partitioning of 24 trace elements: Contributions to Mineralogy and Petrology, v. 113, p. 1–8, https://doi.org/10.1007/BF00320827.

Herzberg, C., Cabral, R.A., Jackson, M.G., Vidito, C., Day, J.M.D., and Hauri, E.H., 2014, Phantom Archean crust in Mangaia hotspot lavas and the meaning of heterogeneous mantle: Earth and Planetary Science Letters, v. 396, p. 97–106, https://doi.org/10.1016/j.epsl.2014.03.065.

Irvine, T.N.J., and Baragar, W., 1971, A guide to the chemical classification of the common volcanic rocks: Canadian Journal of Earth Sciences, v. 8, p. 523–548, https://doi.org/10.1139/e71-055.

Jahn-Awe, S., Froitzheim, N., Nagel, T.J., Frei, D., Georgiev, N., and Pleuger, J., 2010, Structural and geochronological evidence for Paleogene thrusting in the western Rhodopes, SW Bulgaria: Elements for a new tectonic model of the Rhodope Metamorphic Province: Tectonics, v. 29, https://doi.org/10.1029/2009TC002558.

Jenkin, G.R.T., Ellam, R.M., Rogers, G., and Stuart, F.M., 2001, An investigation of closure temperature of the biotite Rb-Sr system: The importance of cation exchange: Geochimica et Cosmochimica Acta, v. 65, p. 1141–1160, https://doi.org/10.1016/S0016-7037(00)00560-3.

Jolivet, L., and Brun, J.P., 2010, Cenozoic geodynamic evolution of the Aegean: International Journal of Earth Sciences, v. 99, p. 109–138, https://doi.org/10.1007/s00531-008-0366-4.

Jolivet, L., Faccenna, C., Huet, B., Labrousse, L., Le Pourhiet, L., Lacombe, O., Lecomte, E., Burov, E., Denele, Y., Brun, J.-P., et al., 2013, Aegean tectonics: Strain localisation, slab tearing and trench retreat: Tectonophysics, v. 597, p. 1–33, https://doi.org/10.1016/j.tecto.2012.06.011.

Jones, C.E., Tarney, J., Baker, J.H., and Gerouki, F., 1992, Tertiary granitoids of Rhodope, northern Greece: Magmatism related to extensional collapse of the Hellenic Orogen?: Tectonophysics, v. 210, p. 295–314, https://doi.org/10.1016/0040-1951(92)90327-3.

Katerinopoulou, A., Katerinopoulos, A., Voudouris, P., Bieniok, A., Musso, M., and Amthauer, G., 2009, A multi-analytical study of the crystal structure of unusual Ti-Zr-Cr–rich andradite from the Maronia skarn, Rhodope massif, western Thrace, Greece: Mineralogy and Petrology, v. 95, p. 113, https://doi.org/10.1007/s00710-008-0023-4.

Kilias, A., Falalakis, G., Sfeikos, A., Papadimitriou, E., Vamvaka, A., and Gkarlaouni, C., 2013, The Thrace basin in the Rhodope province of NE Greece—A tertiary supradetachment basin and its geodynamic implications: Tectonophysics, v. 595–596, p. 90–105, https://doi.org/10.1016/j.tecto.2012.05.008.

Kokkinakis, A., 1980, Altersbeziehungen zwischen Metamorphosen, mechanischen Deformationen und Intrusionen am Suedrand des Rhodope-Massivs (Makedonien, Griechenland): Geologische Rundschau, v. 69, p. 726–744, https://doi.org/10.1007/BF02104643.

Krenn, K., Bauer, C., Proyer, A., Klötzli, U., and Hoinkes, G., 2010, Tectonometamorphic evolution of the Rhodope orogen: Tectonics, v. 29, https://doi.org/10.1029/2009TC002513.

Krohe, A., and Mposkos, E., 2002, Multiple generations of extensional detachments in the Rhodope Mountains (northern Greece): Evidence of episodic exhumation of high-pressure rocks, *in* Blundell, D.J., Neubauer, F., and von Quadt, A., eds., The Timing and Location of Major Ore Deposits in an Evolving Orogen: Geological Society, London, Special Publication 204, p. 151–178, https://doi.org/10.1144/GSL.SP.2002.204.01.10.

Kydonakis, K., Gallagher, K., Brun, J.-P., Jolivet, M., Gueydan, F., and Kostopoulos, D., 2014, Upper Cretaceous exhumation of the western Rhodope Metamorphic Province (Chalkidiki Peninsula, northern Greece): Tectonics, v. 33, p. 1113–1132, https://doi.org/10.1002/2014TC003572.

Kydonakis, K., Brun, J.-P., and Sokoutis, D., 2015, North Aegean core complexes, the gravity spreading of a thrust wedge: Journal of Geophysical Research, Solid Earth, v. 120, p. 595–616, https://doi.org/10.1002/2014JB011601.

Lanzo, G., Di Carlo, I., Pichavant, M., Rotolo, S.G., and Scaillet, B., 2016, Origin of primitive ultra-calcic arc melts at crustal conditions—Experimental evidence on the La Sommata basalt, Vulcano, Aeolian Islands: Journal of Volcanology and Geothermal Research, v. 321, p. 85–101, https://doi.org/10.1016/j.jvolgeores.2016.04.032.

LaTourrette, T., Hervig, R.L., and Holloway, J.R., 1995, Trace element partitioning between amphibole, phlogopite, and basanite melt: Earth and Planetary Science Letters, v. 135, p. 13–30.

Le Pichon, X., and Angelier, J., 1979, The Hellenic arc and trench system: A key to the neotectonic evolution of the eastern Mediterranean area: Tectonophysics, v. 60, p. 1–42, https://doi.org/10.1016/0040-1951(79)90131-8.

Liati, A., and Kreuzer, H., 1990, K-Ar dating of metamorphic and magmatic rocks from the Xanthi and Drama areas, Greek part of the Rhodope zone: European Journal of Mineralogy, v. 2, p. 161.

Liati, A., Gebauer, D., and Wysoczanski, R., 2002, U-Pb SHRIMP-dating of zircon domains from UHP garnet-rich mafic rocks and late pegmatoids in the Rhodope zone (N Greece); Evidence for Early Cretaceous crystallization and Late Cretaceous metamorphism: Chemical Geology, v. 184, p. 281–299, https://doi.org/10.1016/S0009-2541(01)00367-9.

Lipman, P.W., Prostka, H.J., and Christiansen, R.L., 1972, Cenozoic volcanism and plate-tectonic evolution of the Western United States: I. Early and middle Cenozoic: Philosophical Transactions of the Royal Society A, Mathematical, Physical and Engineering Sciences, v. 271, p. 217–248.

Lips, A.L.W., White, S.H., and Wijbrans, J.R., 2000, Middle-late Alpine thermotectonic evolution of the southern Rhodope Massif, Greece: Geodinamica Acta, v. 13, p. 281–292, https://doi.org/10.1080/09853111.2000.11105375.

Lister, G.S., Banga, G., and Feenstra, A., 1984, Metamorphic core complexes of Cordilleran type in the Cyclades, Aegean Sea, Greece: Geology, v. 12, p. 221–225, https://doi.org/10.1130/0091-7613(1984)12<221:MCCOCT>2.0.CO;2.

Lledo, H.L., and Jenkins, D.M., 2007, Experimental investigation of the upper thermal stability of Mg-rich actinolite; implications for Kiruna-type iron deposits: Journal of Petrology, v. 49, p. 225–238, https://doi.org/10.1093/petrology/egm078.

Marchev, P., Kaiser-Rohrmeier, M., Heinrich, C., Ovtcharova, M., von Quadt, A., and Raicheva, R., 2005, 2: Hydrothermal ore deposits related to post-orogenic extensional magmatism and core complex formation: The Rhodope Massif of Bulgaria and Greece: Ore Geology Reviews, v. 27, p. 53–89, https://doi.org/10.1016/j.oregeorev.2005.07.027.

Marchev, P., Von Quadt, A., Peytcheva, I., and Ovtcharova, M., 20016, The age and origin of thhe Chuchuliga and Rozino granites, Eastern Rhodopes: Proceedings of the Annual Conference of the Bulgaria Geological Society Geosciences 2006, p. 213–216.

Marchev, P., Kibarov, P., Spikings, R.A., Ovtcharova, M., Marton, I., and Moritz, R., 2010, $^{40}Ar/^{39}Ar$ and U-Pb geochronology of the Iran Tepe volcanic complex, Eastern Rhodopes: Geologica Balcanica, v. 39, p. 3–12.

Marchev, P., Georgiev, S., Raicheva, R., Peytcheva, I., von Quadt, A., Ovtcharova, M., and Bonev, N., 2013, Adakitic magmatism in post-collisional setting: An example from the Early–Middle Eocene Magmatic Belt in Southern Bulgaria and Northern Greece: Lithos, v. 180–181, p. 159–180, https://doi.org/10.1016/j.lithos.2013.08.024.

Márton, I., Moritz, R., and Spikings, R., 2010, Application of low-temperature thermochronology to hydrothermal ore deposits: Formation, preservation and exhumation of epithermal gold systems from the Eastern Rhodopes, Bulgaria: Tectonophysics, v. 483, p. 240–254, https://doi.org/10.1016/j.tecto.2009.10.020.

Mattinson, J.M., 2005, Zircon U-Pb chemical abrasion ("CA-TIMS") method: Combined annealing and multi-step partial dissolution analysis for improved precision and accuracy of zircon ages: Chemical Geology, v. 220, p. 47–66, https://doi.org/10.1016/j.chemgeo.2005.03.011.

Mavroudchiev, B., Nedyalkov, R., Eleftheriadis, G., Soldatos, T., and Christofides, G., 1993, Tertiary plutonic rocks from East Rhodope in Bulgaria and Greece: Bulletin of the Geological Society of Greece, v. 27, p. 643–660.

McKenzie, D., and Bickle, M.J., 1988, The volume and composition of melt generated by extension of the lithosphere: Journal of Petrology, v. 29, p. 625–679, https://doi.org/10.1093/petrology/29.3.625.

McKenzie, D.A.N., and O'Nions, R.K., 1991, Partial melt distributions from inversion of rare earth element concentrations: Journal of Petrology, v. 32, p. 1021–1091, https://doi.org/10.1093/petrology/32.5.1021.

Meen, J.K., 1987, Formation of shoshonites from calcalkaline basalt magmas: Geochemical and experimental constraints from the type locality: Contributions to Mineralogy and Petrology, v. 97, p. 333–351, https://doi.org/10.1007/BF00371997.

Meinhold, G., and Kostopoulos, D.K., 2013, The Circum-Rhodope Belt, northern Greece: Age, provenance, and tectonic setting: Tectonophysics, v. 595–596, p. 55–68, https://doi.org/10.1016/j.tecto.2012.03.034.

Meinhold, G., Reischmann, T., Kostopoulos, D., Frei, D., and Larionov, A.N., 2010, Mineral chemical and geochronological constraints on the age and provenance of the eastern Circum-Rhodope Belt low-grade metasedimentary rocks, NE Greece: Sedimentary Geology, v. 229, p. 207–223, https://doi.org/10.1016/j.sedgeo.2010.06.007.

Melfos, V., Vavelidis, M., Christofides, G., and Seidel, E., 2002, Origin and evolution of the Tertiary Maronia porphyry copper-molybdenum deposit, Thrace, Greece: Mineralium Deposita, v. 37, p. 648–668, https://doi.org/10.1007/s00126-002-0277-4.

Melfos, V., and Voudouris, P., 2016, Fluid evolution in Tertiary magmatic-hydrothermal ore systems at the Rhodope metallogenic province, NE Greece. A review: Geologia Croatica, v. 69, p. 157–167, https://doi.org/10.4154/GC.2016.12.

Melfos, V., and Voudouris, P., 2017, Cenozoic metallogeny of Greece and potential for precious, critical and rare metals exploration: Ore Geology Reviews, v. 89, p. 1030–1057, https://doi.org/10.1016/j.oregeorev.2017.05.029.

Meyer, W., 1968, Alterstellung des Plutonismus im Südteil der Rila-Rhodope-Masse (Nordgriechenland): Geologica et Palaeontologica, v. 2, p. 173–192.

Mountrakis, D., 2006, Tertiary and Quaternary tectonics of Greece, *in* Dilek, Y., and Pavlides, S., eds., Postcollisional Tectonics and Magmatism in the Mediterranean Region and Asia: Geological Society of America Special Paper 409, p. 125–136, https://doi.org/10.1130/2006.2409(07).

Mposkos, E.D., and Kostopoulos, D.K., 2001, Diamond, former coesite and supersilicic garnet in metasedimentary rocks from the Greek Rhodope: A new ultrahigh-pressure metamorphic province established: Earth and Planetary Science Letters, v. 192, p. 497–506, https://doi.org/10.1016/S0012-821X(01)00478-2.

Mposkos, E., and Wawrzenitz, N., 1995, Metapegmatites and pegmatites bracketing the time of high P-metamorphism in polymetamorphic rocks of the E-Rhodope, N. Greece: Petrological and geochronological constraints: Proceedings, XV Congress of the Carpathian-Balkan Geological Association, Geological Society of Greece Special Publications no. 4, p. 602–608.

Müller, D., and Groves, D.I., 2016, Tectonic settings of potassic igneous rocks, *in* Müller, D., and Groves, I., eds., Potassic Igneous Rocks and Associated Gold-Copper Mineralization: New York, Springer, p. 19–52, https://doi.org/10.1007/978-3-319-23051-1_3.

Mutch, E.J., Blundy, J.D., Tattitch, B.C., Cooper, F.J., and Brooker, R.A., 2016, An experimental study of amphibole stability in low pressure granitic magmas and a Revised Al-in-hornblende geobarometer: Contributions to Mineralogy and Petrology, v. 171, p. 85, https://doi.org/10.1007/s00410-016-1298-9.

Naney, M.T., 1983, Phase equilibria of rock-forming ferromagnesian silicates in granitic systems: American Journal of Science, v. 283, p. 993–1033, https://doi.org/10.2475/ajs.283.10.993.

Nockolds, S.R., 1954, Average chemical compositions of some igneous rocks: Geological Society of America Bulletin, v. 65, p. 1007–1032, https://doi.org/10.1130/0016-7606(1954)65[1007:ACOSOI]2.0.CO;2.

Ovtcharova, M., Quadt, A.V., Cherneva, Z., Sarov, S., Heinrich, C., and Peytcheva, I., 2004, U-Pb dating of zircon and monazite from granitoids and migmatites in the core and eastern periphery of the Central Rhodopean Dome, Bulgaria: Geochimica et Cosmochimica Acta, v. 68, p. A664.

Papadopoulou, L., Christofides, G., Koroneos, A., Bröcker, M., Soldatos, T., and Eleftheriadis, G., 2004, Evolution and origin of the Maronia pluton, Thrace, Greece: Proceedings of the 10th International Congress, Bulletin of the Geological Society of Greece, v. 36, p. 568–577.

Pearce, J.A., and Peate, D.W., 1995, Tectonic implications of the composition of volcanic arc magmas: Annual Review of Earth and Planetary Sciences, v. 23, p. 251–285, https://doi.org/10.1146/annurev.ea.23.050195.001343.

Peccerillo, A., and Taylor, S.R., 1976, Geochemistry of Eocene calc-alkaline volcanic rocks from the Kastamonu area, northern Turkey: Contributions to Mineralogy and Petrology, v. 58, p. 63–81, https://doi.org/10.1007/BF00384745.

Peccerillo, A., De Astis, G., Faraone, D., Forni, F., and Frezzotti, M.L., 2013, Compositional variations of magmas in the Aeolian arc: Implications for petrogenesis and geodynamics, *in* Lucchi, F., Peccerillo, A., Keller, J., Tranne, C.A. and Rossi, P.L., eds., The Aeolian Islands Volcanoes: Geological Society, London, Memoir 37, p. 491–510, http://dx.doi.org/10.1144/M37.15.

Pe-Piper, G., and Piper, D.J.W., 2001, Late Cenozoic, post-collisional Aegean igneous rocks: Nd, Pb and Sr isotopic constraints on petrogenetic and tectonic models: Geological Magazine, v. 138, p. 653–668.

Pe-Piper, G., and Piper, D.J.W., 2006, Unique features of the Cenozoic igneous rocks of Greece: Geological Society of America Special Paper 409, p. 259–282, https://doi.org/10.1130/2006.2409(14).

Pe-Piper, G., Piper, D.J.W., Koukouvelas, I., Dolansky, L.M., and Kokkalas, S., 2009, Postorogenic shoshonitic rocks and their origin by melting underplated basalts: The Miocene of Limnos, Greece: Geological Society of America Bulletin, v. 121, p. 39–54, https://doi.org/10.1130/B26317.1.

Platt, J.P., Behr, W.M., and Cooper, F.J., 2015, Metamorphic core complexes: Windows into the mechanics and rheology of the crust: Journal of the Geological Society, v. 172, p. 9–27, https://doi.org/10.1144/jgs2014-036.

Poli, S., and Schmidt, M.W., 2002, Petrology of subducted slabs: Annual Review of Earth and Planetary Sciences, v. 30, p. 207–235, https://doi.org/10.1146/annurev.earth.30.091201.140550.

Ricou, L.E., Burg, J.P., Godfriaux, I., and Ivanov, Z., 1998, Rhodope and Vardar: The metamorphic and the olistostromic paired belts related to the Cretaceous subduction under Europe: Geodinamica Acta, v. 11, p. 285–309, https://doi.org/10.1080/09853111.1998.11105326.

Ring, U., Glodny, J., Will, T., and Thomson, S., 2010, The Hellenic subduction system: high-pressure metamorphism, exhumation, normal faulting, and large-scale extension: Annual Review of Earth and Planetary Sciences, v. 38, p. 45–76, https://doi.org/10.1146/annurev.earth.050708.170910.

Rohrmeier, M.K., von Quadt, A., Driesner, T., Heinrich, C.A., Handler, R., Ovtcharova, M., Ivanov, Z., Petrov, P., Sarov, S., and Peytcheva, I., 2013, Post-orogenic extension and hydrothermal ore formation: High-precision geochronology of the Central Rhodopian Metamorphic Core Complex (Bulgaria-Greece): Economic Geology and the Bulletin of the Society of Economic Geologists, v. 108, p. 691–718, https://doi.org/10.2113/econgeo.108.4.691.

Sahy, D., Condon, D.J., Terry, D.O., Fischer, A.U., and Kuiper, K.F., 2015, Synchronizing terrestrial and marine records of environmental change across the Eocene–Oligocene transition: Earth and Planetary Science Letters, v. 427, p. 171–182, https://doi.org/10.1016/j.epsl.2015.06.057.

Scaillet, B., Holtz, F., and Pichavant, M., 2016, Experimental constraints on the formation of silicic magmas: Elements, v. 12, p. 109–114, https://doi.org/10.2113/gselements.12.2.109.

Schmid, S.M., Bernoulli, D., Fügenschuh, B., Matenco, L., Schefer, S., Schuster, R., Tischler, M., and Ustaszewski, K., 2008, The Alpine-Carpathian-Dinaridic orogenic system: Correlation and evolution of tectonic units: Swiss Journal of Geosciences, v. 101, p. 139–183, https://doi.org/10.1007/s00015-008-1247-3.

Seghedi, I., Downes, H., Szakács, A., Mason, P.R.D., Thirlwall, M.F., Roşu, E., Pécskay, Z., Márton, E., and Panaiotu, C., 2004, Neogene–Quaternary magmatism and geodynamics in the Carpathian–Pannonian region: A synthesis: Lithos, v. 72, p. 117–146, https://doi.org/10.1016/j.lithos.2003.08.006.

Siron, C.R., Thompson, J.F.H., Baker, T., Friedman, R., Tsitsanis, P., Russell, S., Randall, S., and Mortensen, J., 2016, Magmatic and metallogenic framework of Au-Cu porphyry and polymetallic carbonate-hosted replacement deposits of the Kassandra mining district, Northern Greece: Society of Economic Geologists Special Publication 19, p. 29–55.

Smith, A.G., and Moores, E.M., 1974, Hellenides, *in* Spencer, A.M., ed., Mesozoic–Cenozoic Orogenic Belts: Geological Society, London, Special Publication 4, p. 159–185, https://doi.org/10.1144/GSL.SP.2005.004.01.09.

Smith, D.J., 2014, Clinopyroxene precursors to amphibole sponge in arc crust: Nature Communications, v. 5, p. 1–6, https://doi.org/10.1038/ncomms5329.

Soldatos, T., Koroneos, A., Kamenov, B.K., Peytcheva, I., von Quadt, A., Christofides, G., Zheng, X., and Sang, H., 2008, New U-Pb and Ar-Ar mineral ages for the Barutin-Buynovo-Elatia-Skaloti-Paranesti batholith (Bulgaria and Greece): Refinement of its debatable age: Bulletin of Geochemistry, Mineralogy and Petrology, v. 46, p. 85–102.

Tatsumi, Y., 1989, Migration of fluid phases and genesis of basalt magmas in subduction zones: Journal of Geophysical Research, Solid Earth, v. 94, p. 4697–4707, https://doi.org/10.1029/JB094iB04p04697.

Teyssier, C., and Whitney, D.L., 2002, Gneiss domes and orogeny: Geology, v. 30, p. 1139–1142, https://doi.org/10.1130/0091-7613(2002)030<1139:GDAO>2.0.CO;2.

Turpaud, P., and Reischmann, T., 2010, Characterisation of igneous terranes by zircon dating: Implications for UHP occurrences and suture identification in the Central Rhodope, northern Greece: International Journal of Earth Sciences, v. 99, p. 567–591, https://doi.org/10.1007/s00531-008-0409-x.

van Hinsbergen, D.J.J., Dupont-Nivet, G., Nakov, R., Oud, K., and Panaiotu, C., 2008, No significant post-Eocene rotation of the Moesian Platform and Rhodope (Bulgaria): Implications for the kinematic evolution of the Carpathian and Aegean arcs: Earth and Planetary Science Letters, v. 273, p. 345–358, https://doi.org/10.1016/j.epsl.2008.06.051.

van Hinsbergen, D.J.J., Hafkenscheid, E., Spakman, W., Meulenkamp, J.E., and Wortel, R., 2005, Nappe stacking resulting from subduction of oceanic and continental lithosphere below Greece: Geology, v. 33, p. 325, https://doi.org/10.1130/G20878.1.

von Blanckenburg, F., and Davies, J.H., 1995, Slab breakoff: A model for syncollisional magmatism and tectonics in the Alps: Tectonics, v. 14, p. 120–131, https://doi.org/10.1029/94TC02051.

von Quadt, A., Erni, M., Martinek, K., Moll, M., Peytcheva, I., and Heinrich, C.A., 2011, Zircon crystallization and the lifetimes of ore-forming magmatic-hydrothermal systems: Geology, v. 39, p. 731–734, https://doi.org/10.1130/G31966.1.

von Quadt, A., and Peytcheva, I., 2005, The southern extension of the Srednogorie type Upper Cretaceous magmatism in Rila–western Rhodopes: Constraints from isotope-geochronological and geochemical data: Sofia, Proceedings of the Bulgarian Geological Society Annual Conference (80th Anniversary), p. 113–116.

Voudouris, P., Tarkian, M., and Arikas, K., 2006, Mineralogy of telluride-bearing epithermal ores in the Kassiteres-Sappes area, western Thrace, Greece: Mineralogy and Petrology, v. 87, p. 31–52, https://doi.org/10.1007/s00710-005-0119-z.

Wang, Y., Foley, S.F., and Prelević, D., 2017, Potassium-rich magmatism from a phlogopite-free source: Geology, v. 45, p. 467–470, https://doi.org/10.1130/G38691.1.

Wang, M., Song, S., Niu, Y., and Su, L., 2014, Post-collisional magmatism: Consequences of UHPM terrane exhumation and orogen collapse, N. Qaidam UHPM belt, NW China: Lithos, v. 210–211, p. 181–198, https://doi.org/10.1016/j.lithos.2014.10.006.

Wawrzenitz, N., and Krohe, A., 1998, Exhumation and doming of the Thasos metamorphic core complex (S Rhodope, Greece): Structural and geochronological constraints: Tectonophysics, v. 285, p. 301–332, https://doi.org/10.1016/S0040-1951(97)00276-X.

Wawrzenitz, N., and Mposkos, E., 1997, First evidence for Lower Cretaceous HP/HT-metamorphism in the eastern Rhodope, North Aegean region, north-east Greece: European Journal of Mineralogy, v. 9, no. 3, p. 659–664, https://doi.org/10.1127/ejm/9/3/0659.

Wernicke, B.P., England, P.C., Sonder, L.J., and Christiansen, R.L., 1987, Tectonomagmatic evolution of Cenozoic extension in the North American Cordillera, *in* Coward, M.P., Dewey, J.F., and Hancock, P.L, eds., Continental Extensional Tectonics: Geological Society, London, Special Publication 28, p. 203–221, https://doi.org/10.1144/GSL.SP.1987.028.01.15.

Whitney, D.L., Teyssier, C., Rey, P., and Roger Buck, W., 2013, Continental and oceanic core complexes: Geological Society of America Bulletin, v. 125, p. 273–298, https://doi.org/10.1130/B30754.1.

Zagorchev, I., Moorbath, S., and Lilov, P., 1987, Radiogeochronological data on the Alpine igneous activity in the western part of the Rhodope Massif: Geologica Balcanica, v. 17, p. 59–71.

Zagorchev, I., Academy, B., View, R.M., and Zagorchev, I., 2014, Rubidium-strontium isotopic data for Vitosa Pluton, Srednogorie Zone: Geologica Balcanica, v. 17, p. 43–48.

MANUSCRIPT RECEIVED 17 JANUARY 2018
REVISED MANUSCRIPT RECEIVED 14 MARCH 2018
MANUSCRIPT ACCEPTED 16 APRIL 2018